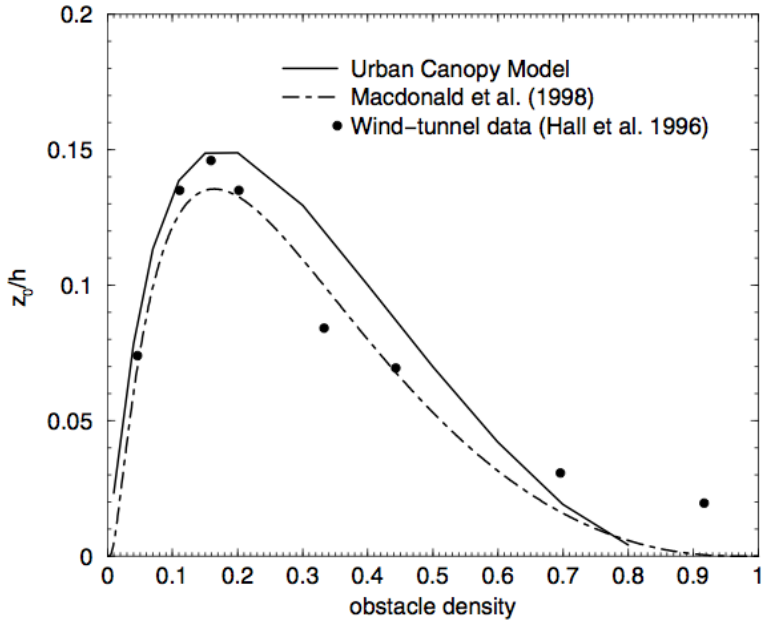

Fig 2.1. Variation of the roughness length and displacement height with packing density for a regular array of cubes. Solid line: canopy model of Belcher & Coceal (2004); dashed line: model of Macdonald (1998); symbols: wind tunnel measurements of Hall et al (1996). Figure adapted from Coceal & Belcher (2004).

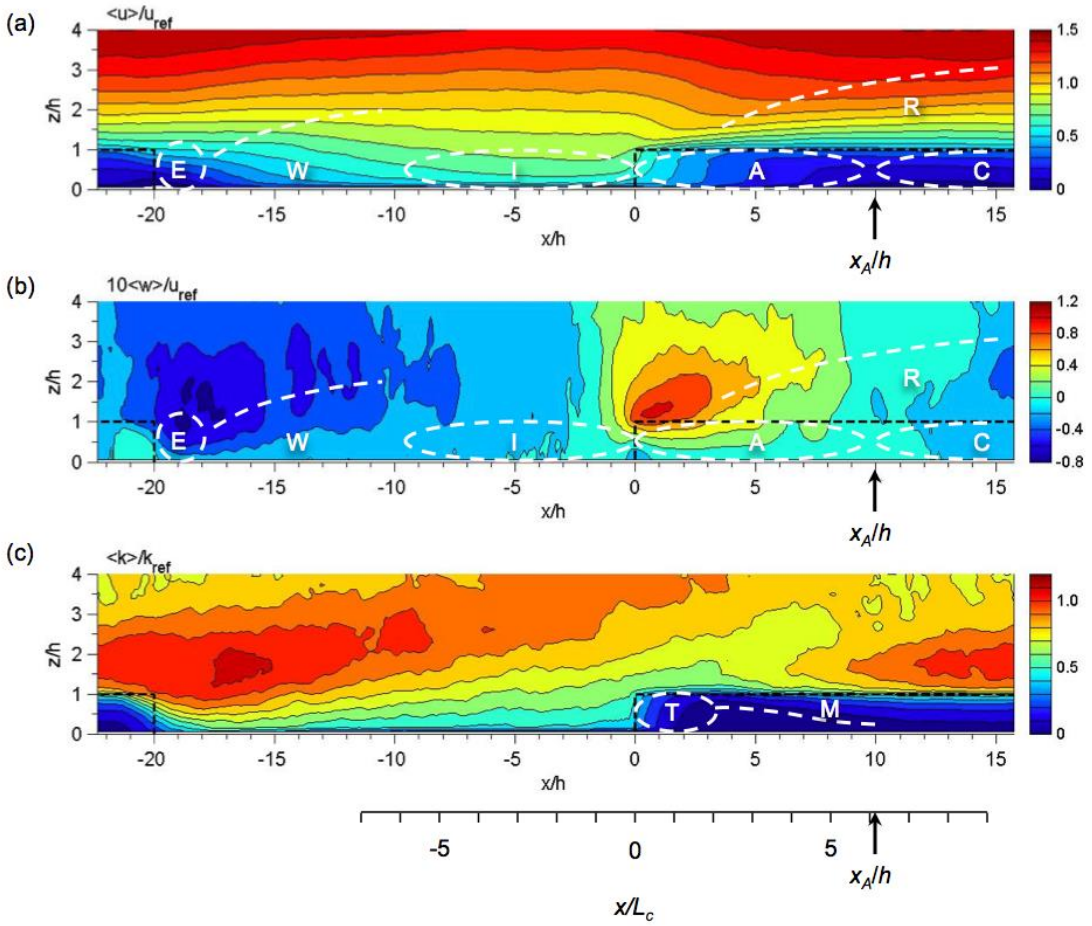

Figure 2.2. Contour plots of the evolution of (a) mean streamwise velocity, (b) mean vertical velocity and (c) turbulent kinetic energy across a forest edge from the LES of Dupont & Brunet (2008). The domain is periodic in the x-direction. The black dashed lines mark the location of the canopy. Overlain are white dashed lines indicating a schematic of the adjustment of the flow (adapted from Belcher et al 2003). Adjustment of the mean flow is indicated in (a) and (b): I: Impact region; A: Adjustment region; C: Canopy flow region; R: Roughness change region; E: Exit region; W: Wake region. Adjustment of the turbulence is indicated in (c): T: Turbulence impact region; M: mixing-layer region. See text for details. Figure replotted from the original data.

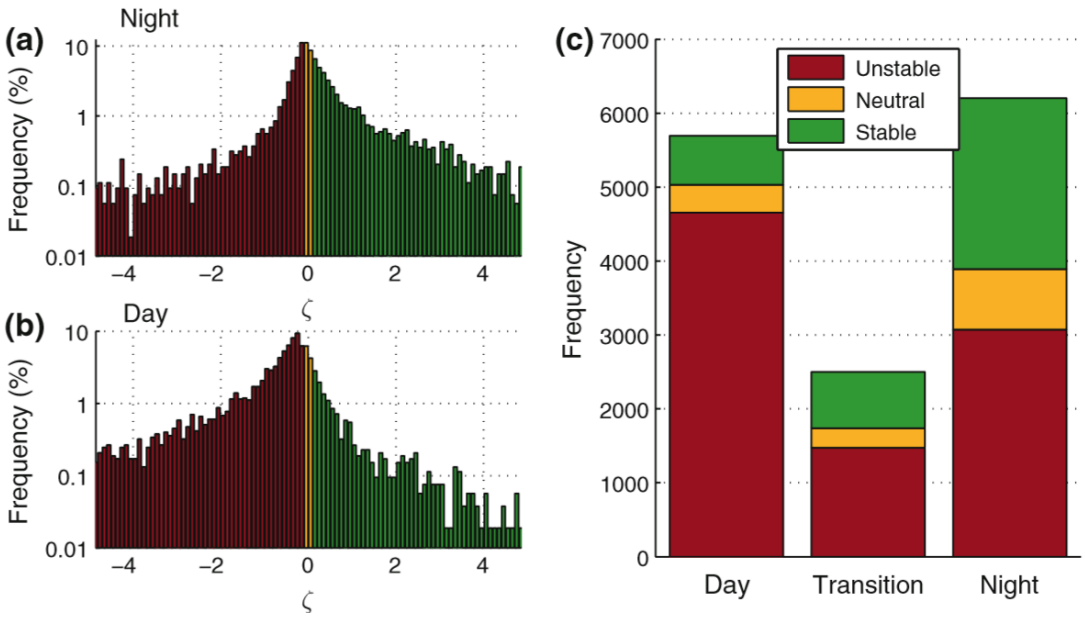

Fig. 2.3. Frequency histogram of the stability parameter (ζ) in 0.1 bins for night time (a) and daytime (b); and frequency of stability classes categorized by period of day (c), transition period was defined as 2 hours centred on sunrise or sunset, based on solar geometry. There were more night time than daytime data due to there being more winter than summer months in the dataset. All data included (i.e. 6446.5h between October 2006 and May 2008). Taken from Wood et al (2010)

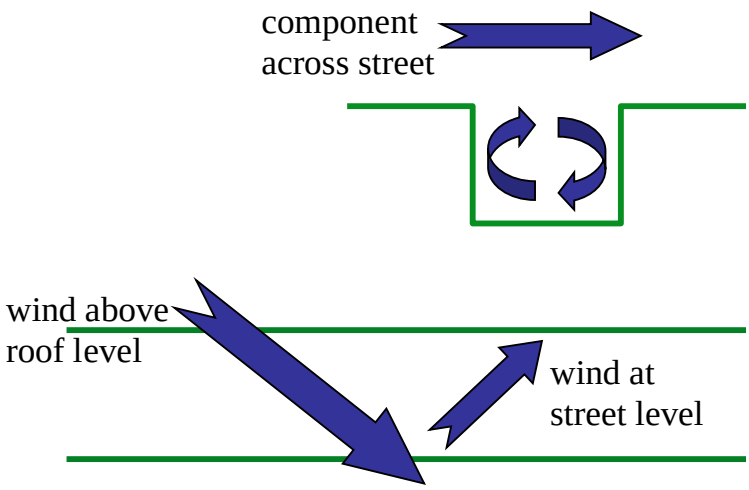

Figure 3.1. The development of a helical recirculating flow in a long street canyon with the wind at incidence to the canyon axis. The flow along the street is driven by the component of the external flow in that direction; the component perpendicular to the street drives the circulation.

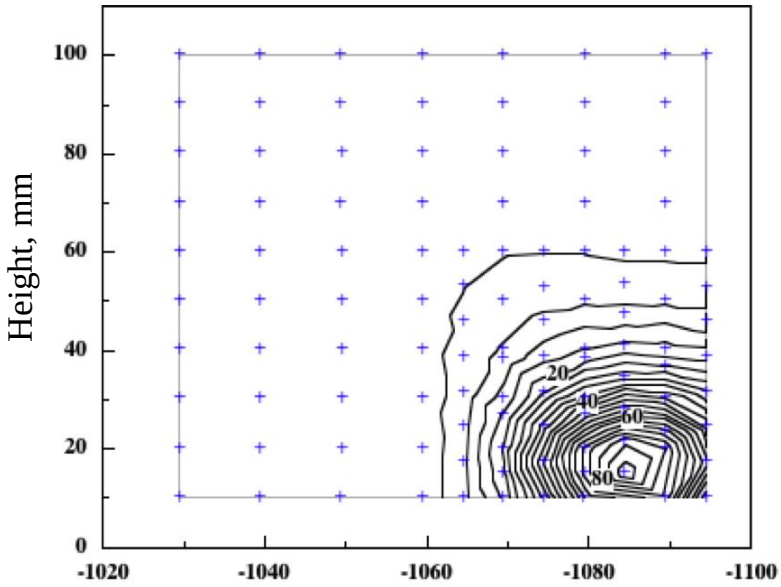

a) Distance from source = 0.8*W*

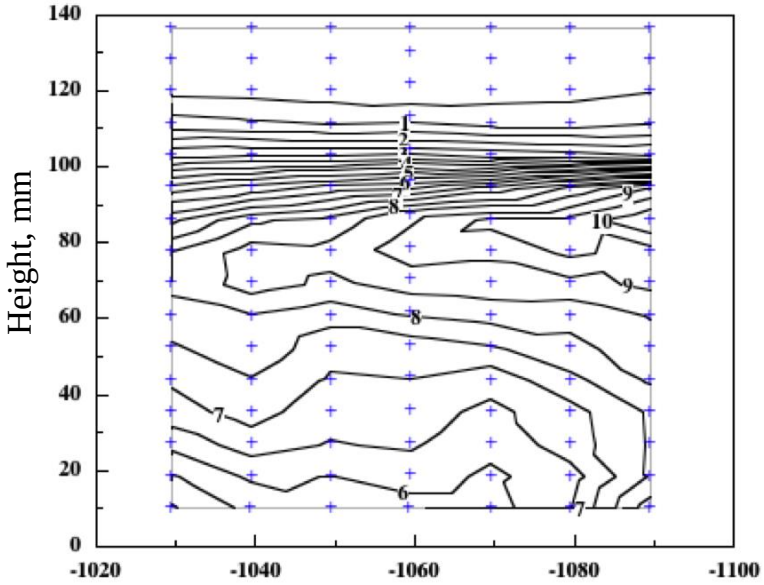

b) Distance from source = 3.5*W*

Figure 3.2. Wind tunnel measurements of dimensionless mean concentration contours in a street canyon downwind of a ground level emission in the centre of the street; wind at 45˚ to canyon axis; a) fetch along street from source = 0.8*W*; b) 3.5*W*. (unpublished DAPPLE data)

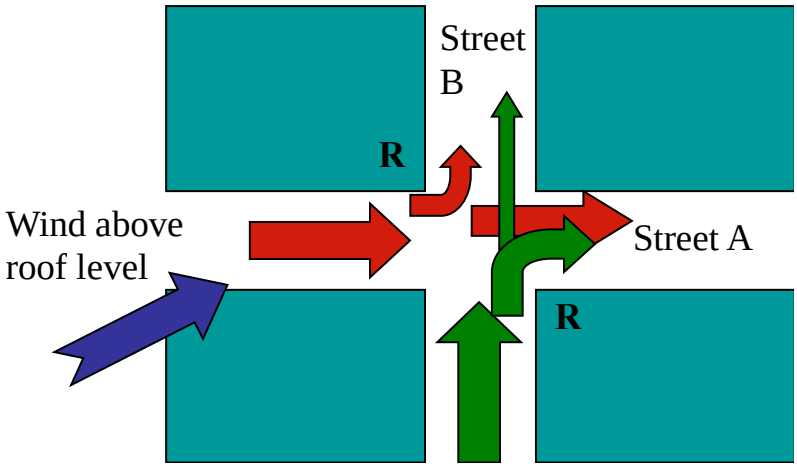

Figure 3.3. Flow and pollutant exchanges at a simple intersection with the wind at incidence to the street axes. This example illustrates the case where the flow along Street A is stronger than that along B. This deflects much of the flow from B into A, though a fraction continues along B at a higher level. Most of the flow in A continues along that street but is deflected to one side. Corner vortices form at R in Streets A and B.

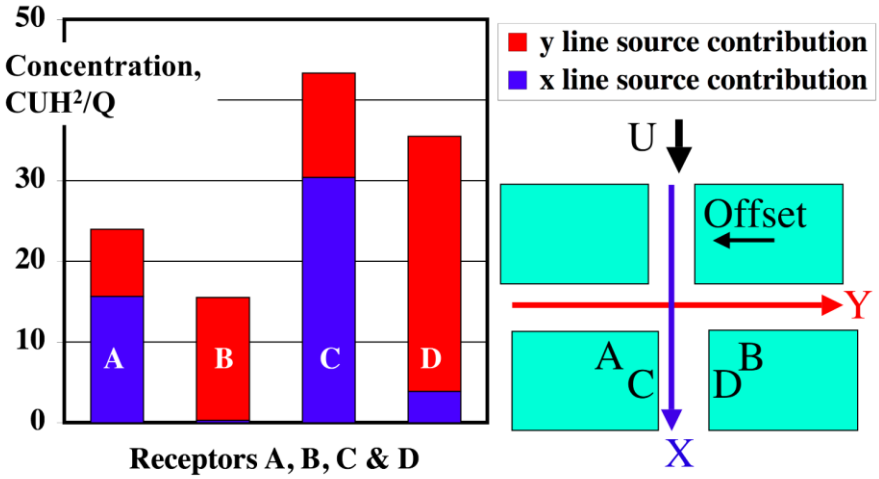

Figure 3.4. Pollutant exchanges between streets at an intersection. The wind is aligned with Street X and perpendicular to Y. A small offset in the alignment of the buildings creates a situation similar to that previously depicted for a wind at incidence. Pollutant from the Street X (north) is deflected into A (west) so that the largest contribution to the concentration at A is from X, whereas at B, in Street Y (east), there is no contribution for X. A similar circumstance holds at C and D in Street X (south). Based on wind tunnel data from Robins et al (2002).

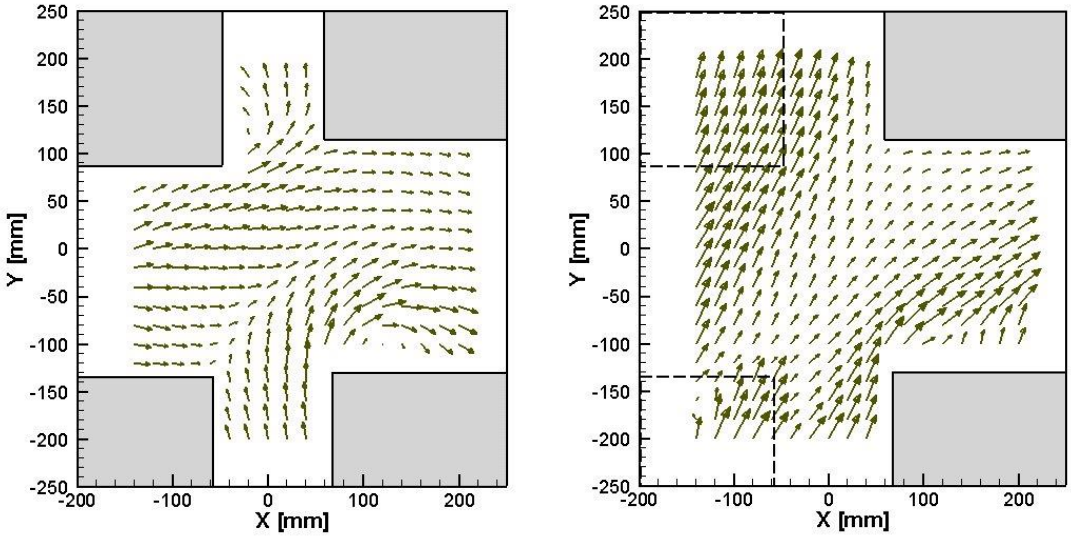

a) Velocity vectors in horizontal planes at 5m (left) and 20m (right) above street level

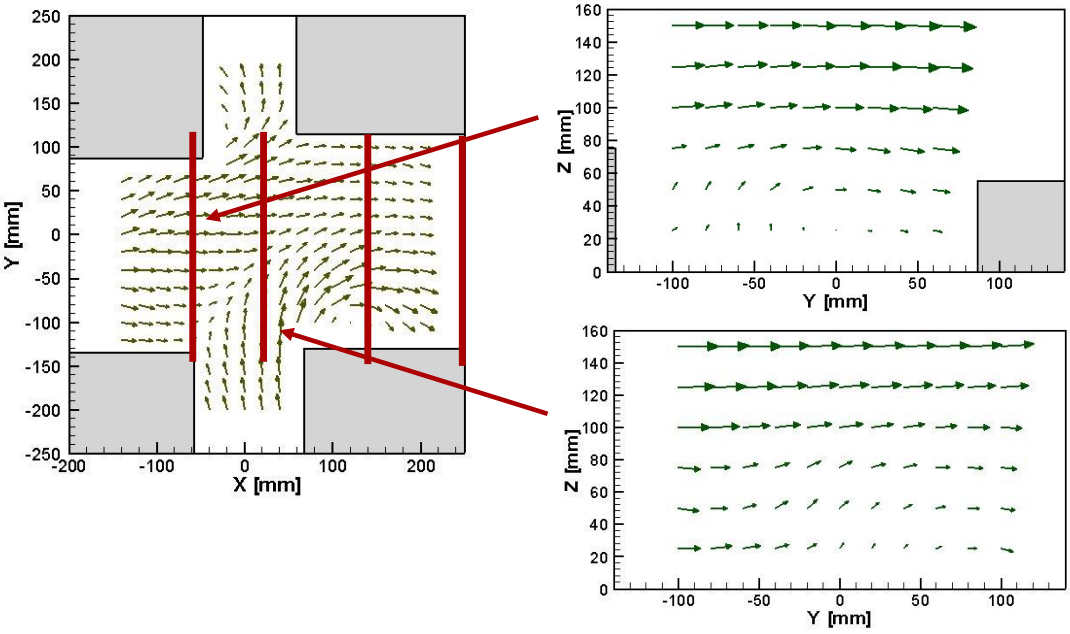

b) Velocity vectors in horizontal plane at 5m above street level (left) and in vertical planes at the intersection (right)

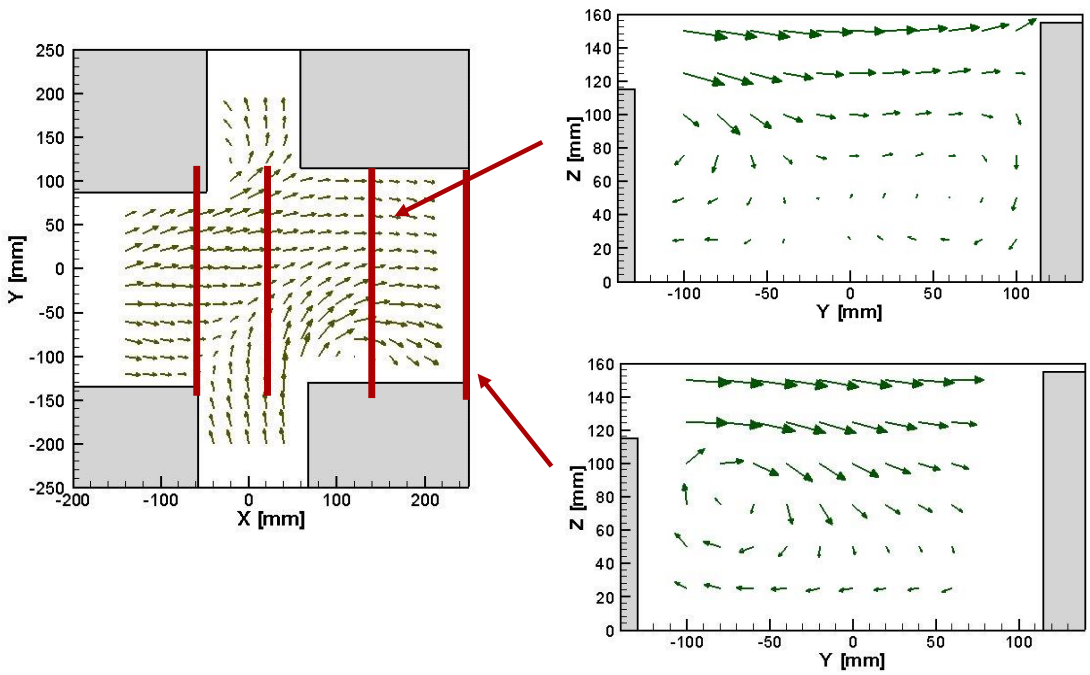

c) Velocity vectors in horizontal plane at 5m above street level (left) and in vertical planes downwind of the intersection (right)

Figure 3.5. The mean velocity field at the intersection between Marylebone Road (x-street) and Gloucester Place (y-street). Wind tunnel data from Carpentieri et al., 2009. a) horizontal planes at the equivalent heights of 5 and 20m; b) and c) the horizontal plane at 5m and a section of vertical planes along Marylebone Road.

Figure 3.6. Smoke visualisation of pollutant exchanges at intersection in the DAPPLE field site in central London. False coloured image derived from wind tunnel flow visualisation study. The illumination is concentrated on the street canyons and pollutant that has been transferred to the external flow is not visible in this image. The source is at the point S and the wind at incidence to the street network. (DAPPLE, 2011)

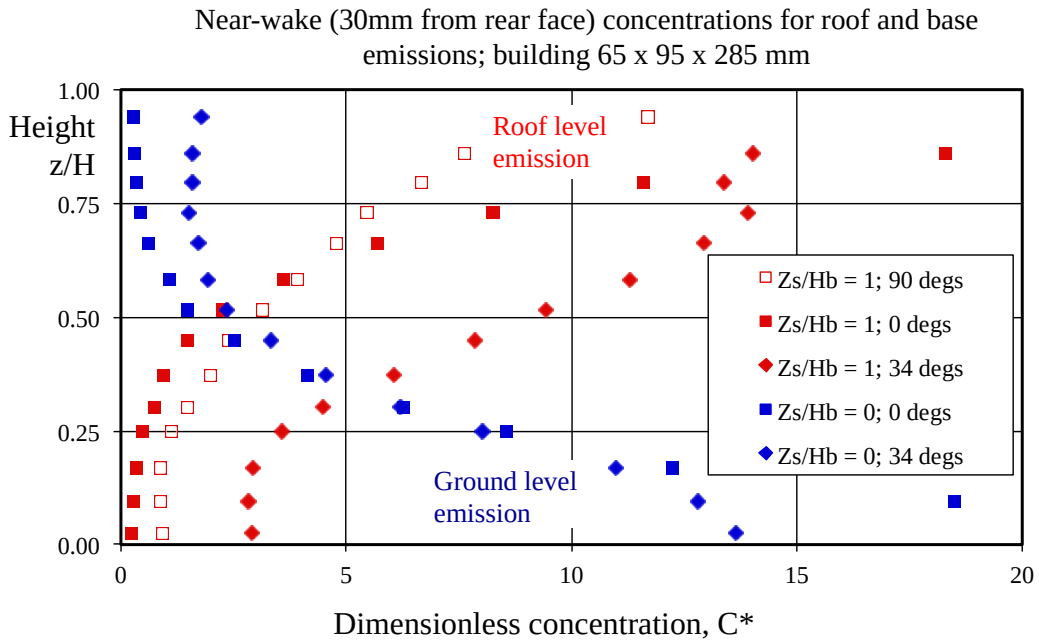

Figure 3.7. Wind tunnel measurements of vertical profiles of dimensionless mean concentration 30mm behind a 285mm tall building, 65x95mm in plan for roof and ground level emissions and three wind directions (unpublished EnFlo wind tunnel data).

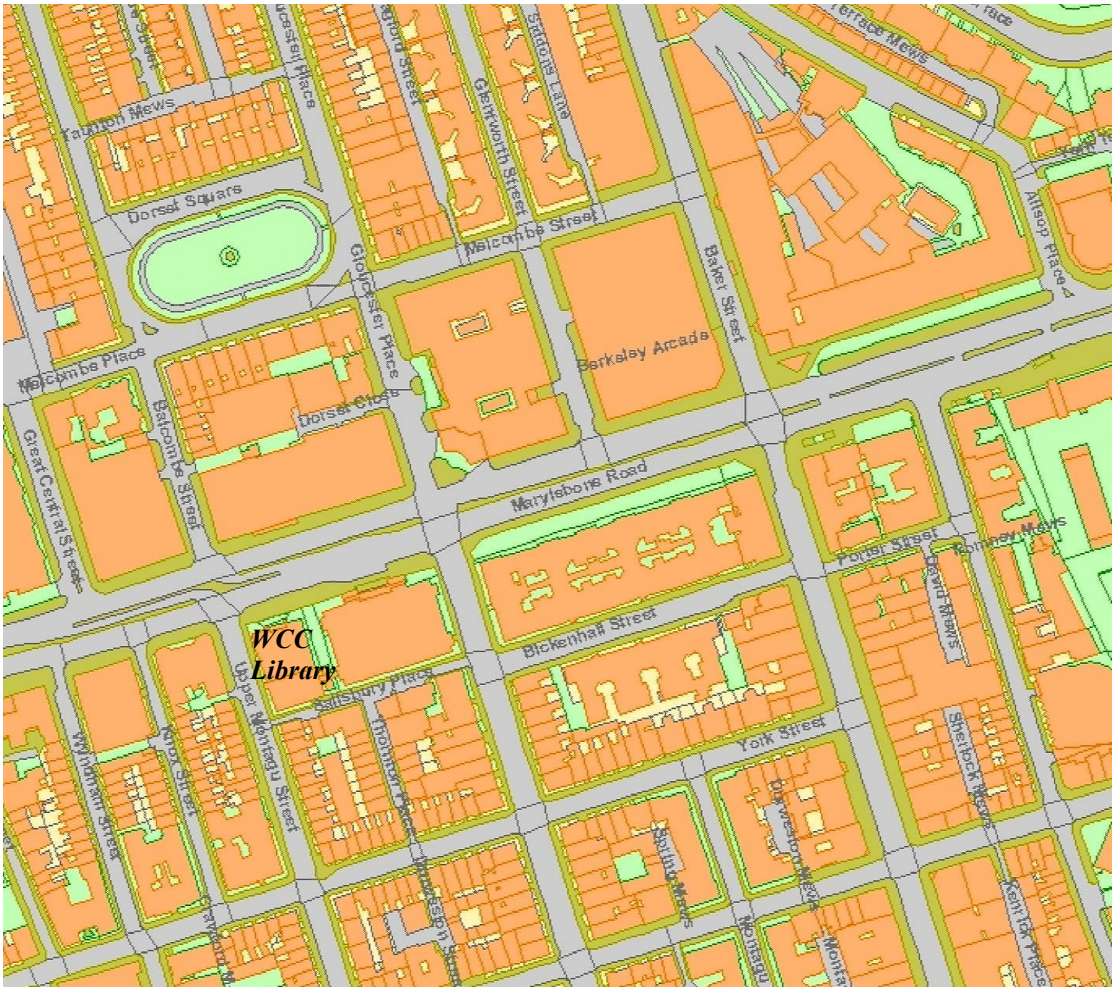

Figure 3.8. Plan of DAPPLE field site including street names and location of WCC Library (site of roof-top reference wind measurement).

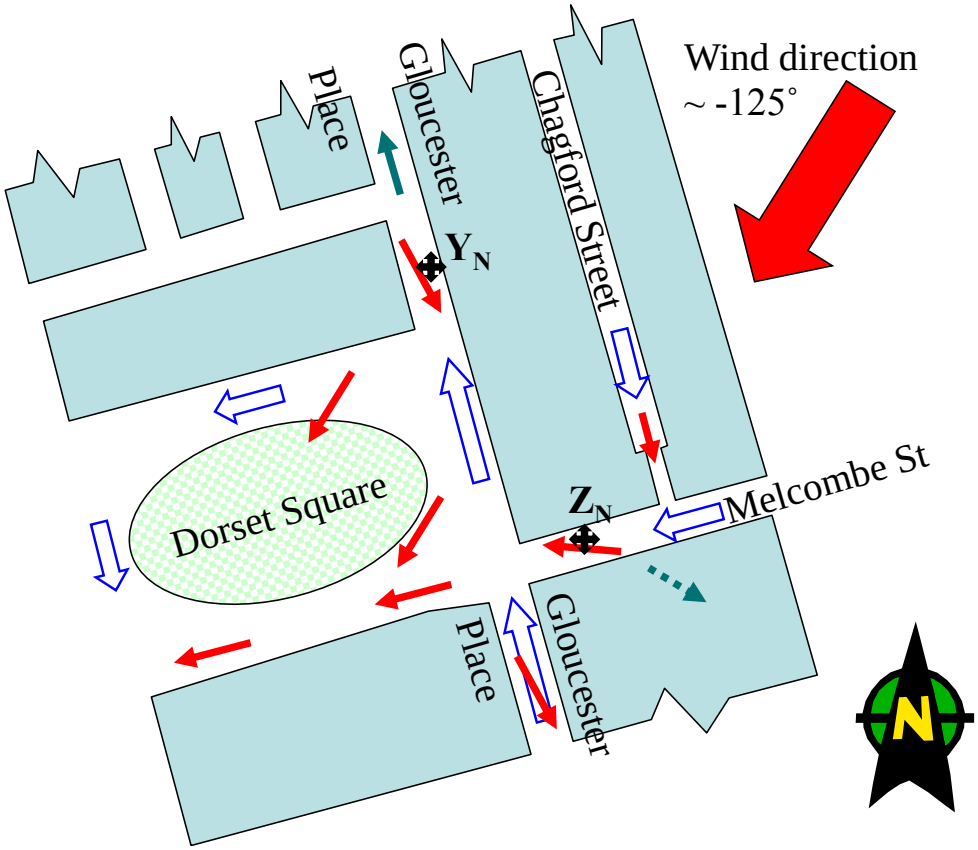

Figure 3.9. Approximate street arrangement in vicinity of Sources Y and Z on Days 2 and 3. Source positions are indicated by a labelled star, one-way traffic flows by the open blue arrows. The small red arrows indicate expected directions of the along-street component of local winds in selected streets (for a steady mean flow from the north-east and uniform building heights); the green arrows are the mean directions inferred from tracer movement (dotted lines imply a direction but not necessarily a route). The large red arrow indicates the wind direction above roof level. (DAPPLE 2011).

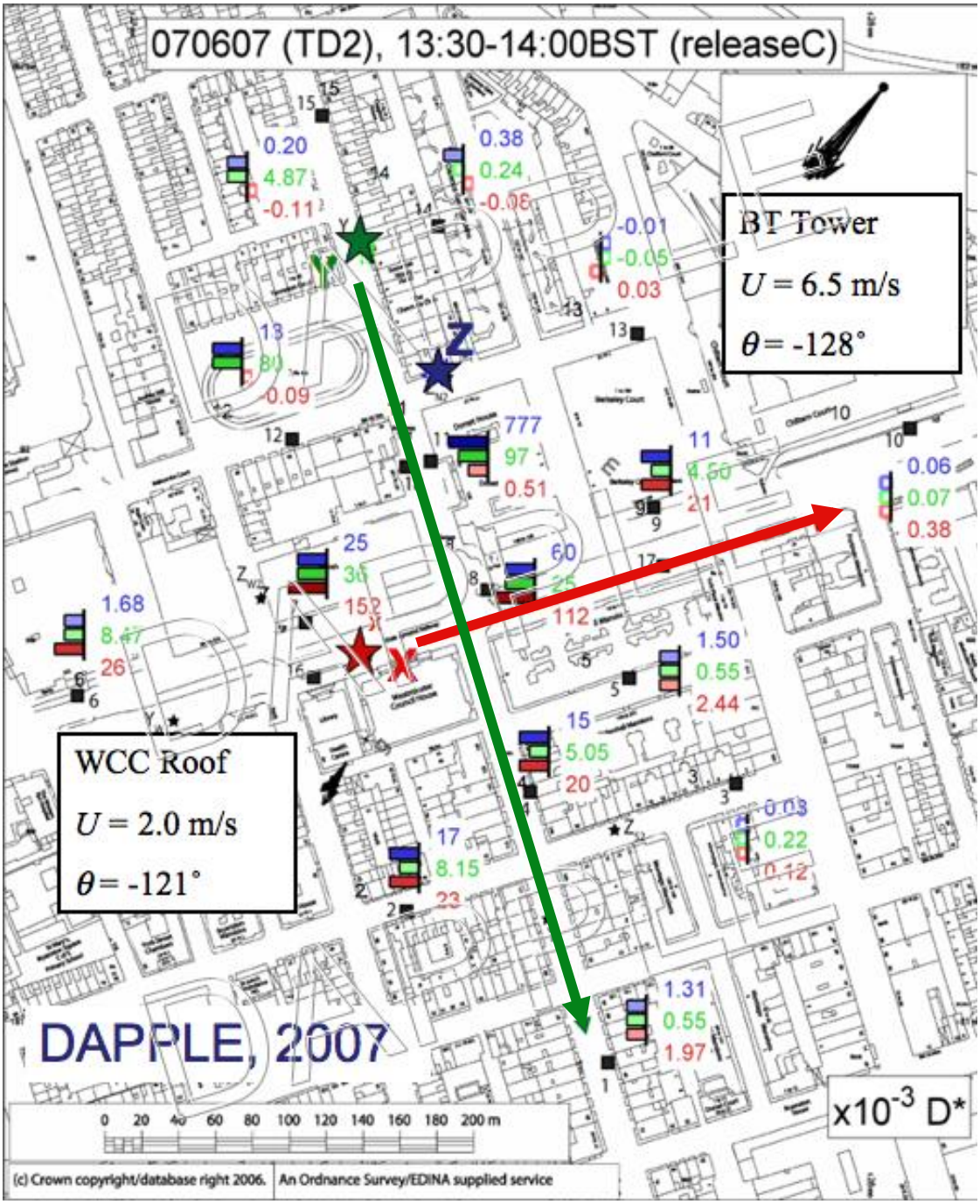

Figure 3.10. Day 2, Experiment C. Dimensionless dosages plotted as 10^3D*, shown as bar charts and numerically with the colours corresponding to the three sources. The wind vectors are two minute averages at WCC Library roof, BT and the source locations, drawn to a common scale. The red arrow shows the direction of upwind dispersion from X and the green arrow rapid lateral dispersion from Y. (DAPPLE, 2011).

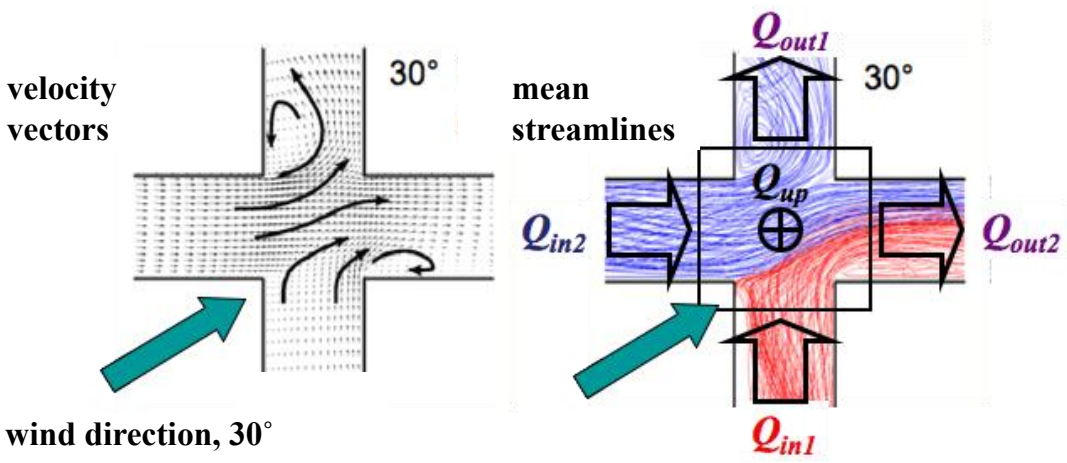

Figure 3.11. Exchanges driven by a diagonally orientated external wind at a simple intersection of two streets, showing the velocity vectors (left) and the flow exchanges (right) near street level (Soulhac, 2000).

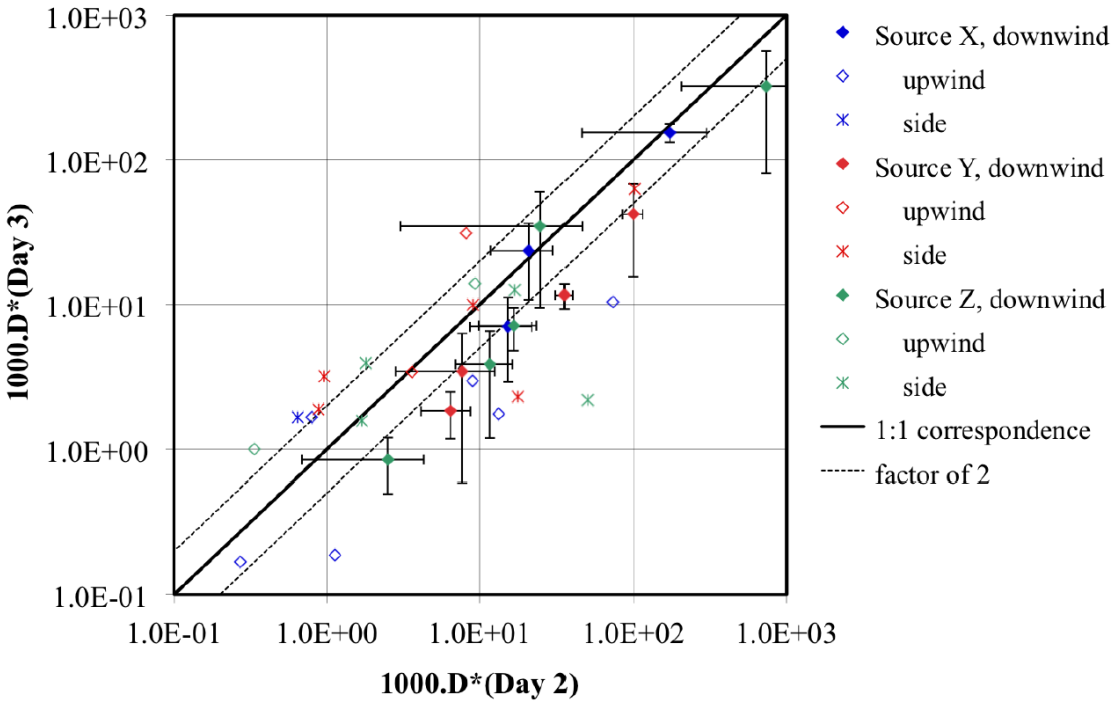

Figure 3.12. Scatter plot of ensemble-average (over four experiments) dimensionless dosages from Days 2 and 3, differentiated according to the receptor location relative to the source. The uncertainty bars for the 'downwind' cases are equal to ± one standard deviation of the ensemble results. (DAPPLE, 2011)

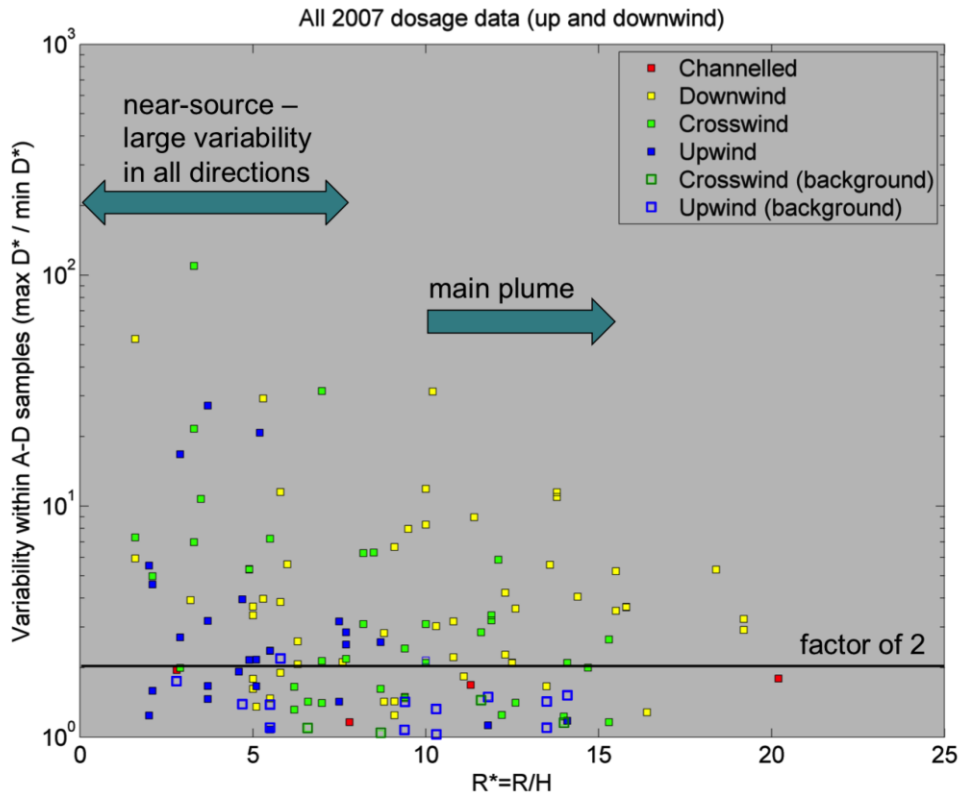

Figure 3.13. Dosage ratios (maximum/minimum) at each site as a function of distance from the source, R/H, where R is the straight line separation and H the average building height. (DAPPLE, 2011)

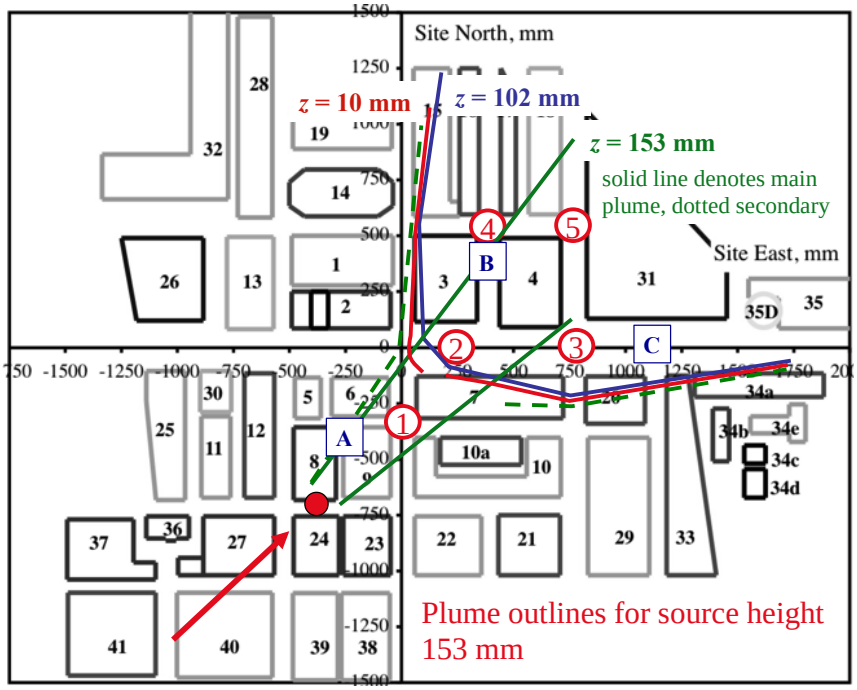

a) Plume outlines for elevated emission at 153mm.

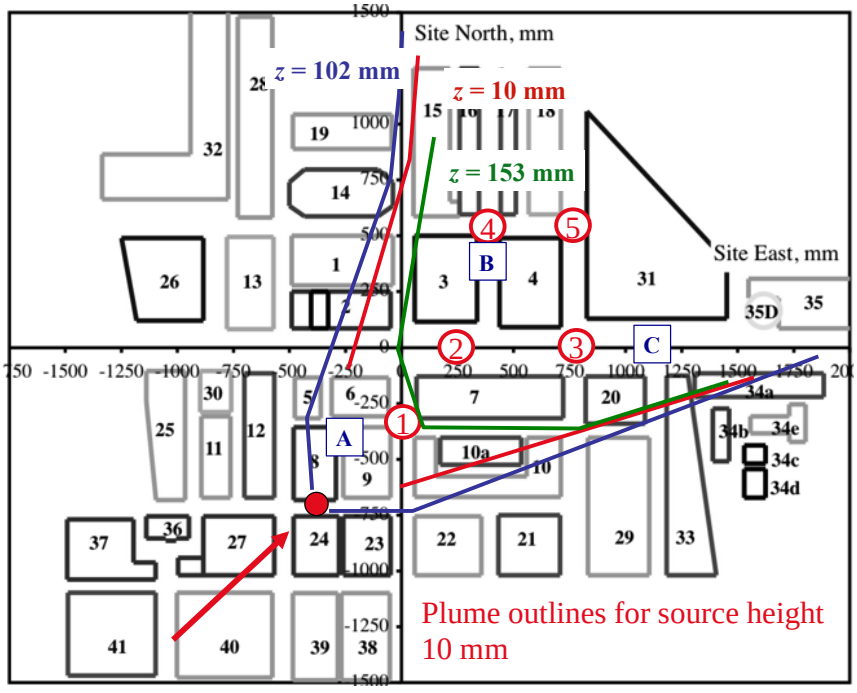

b) Plume outlines for surface emission at 10mm.

Figure 3.14. Wind tunnel plume outlines at heights of 10, 102 and 153mm for emissions at a) 153mm and b) 10mm, wind direction 45˚. The red dot marks the source position; the other marked locations are referred to in the text. (Smethurst, 2012)

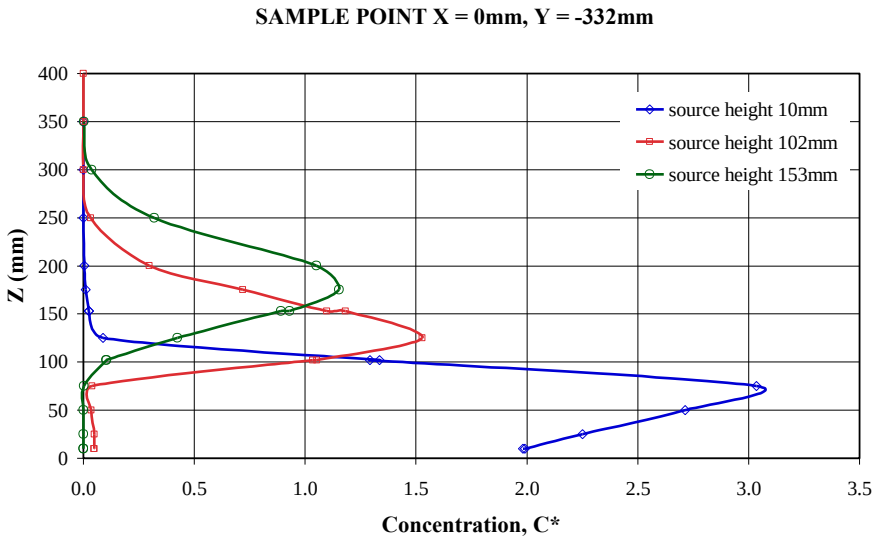

a) Vertical profiles at location 1.

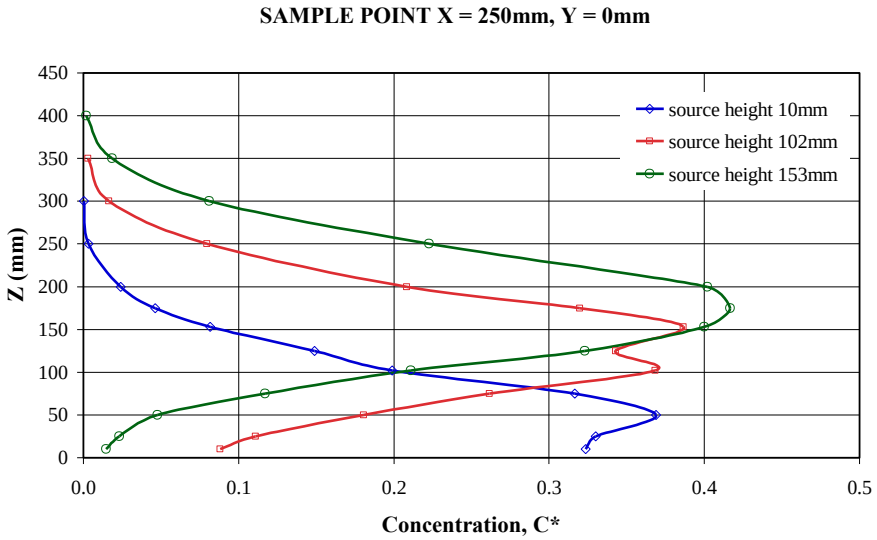

b) Vertical profiles at location 2.

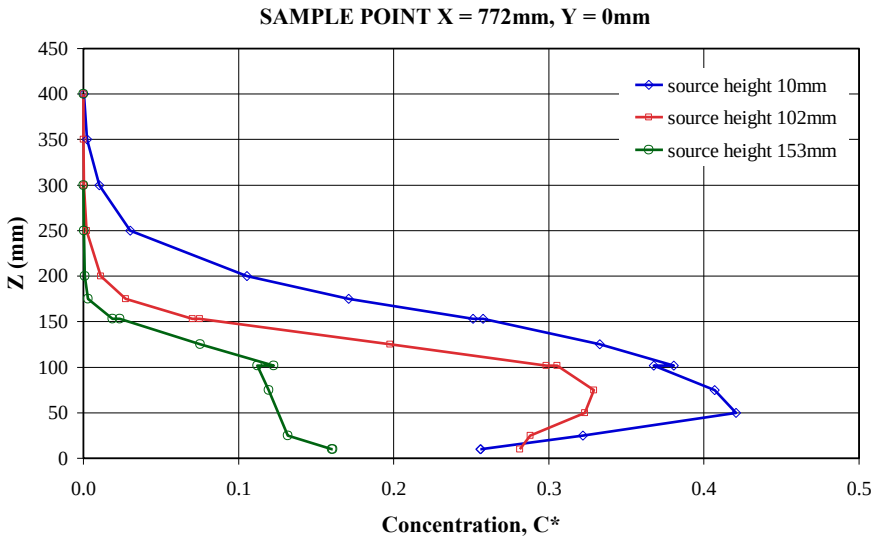

c) Vertical profiles at location 3.

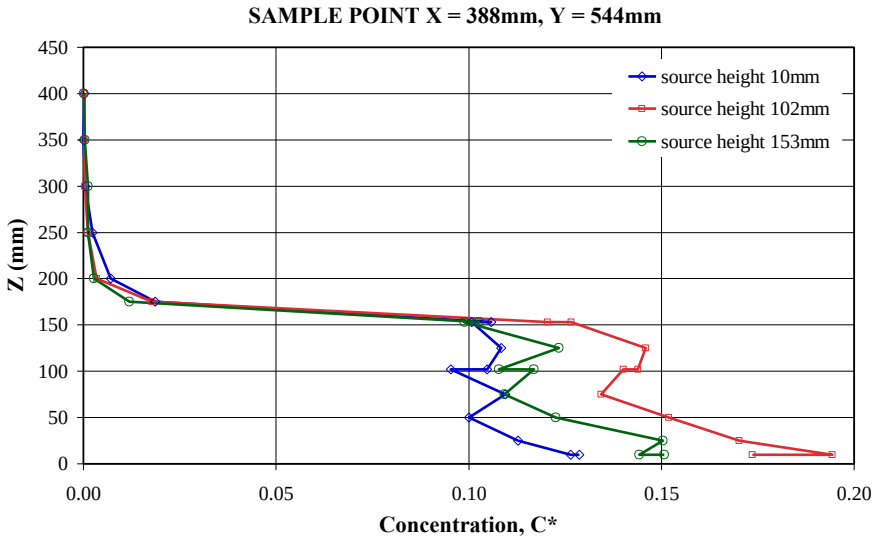

d) Vertical profiles at location 4.

Figure 3.15. Wind tunnel measurements of vertical profiles of dimensionless concentration at four locations for emissions at heights of 10, 102 and 153mm. See Figure E5 for definition of the measurement and source locations. (Smethurst, 2012)

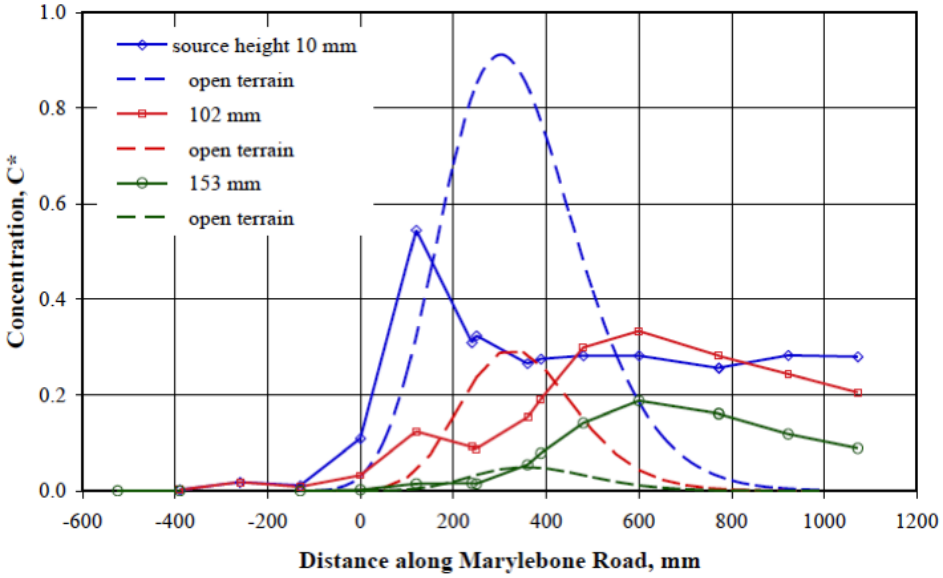

a) Mean dimensionless concentration distributions at street level along Marylebone Road for three source heights compared with data in the undisturbed boundary layer.

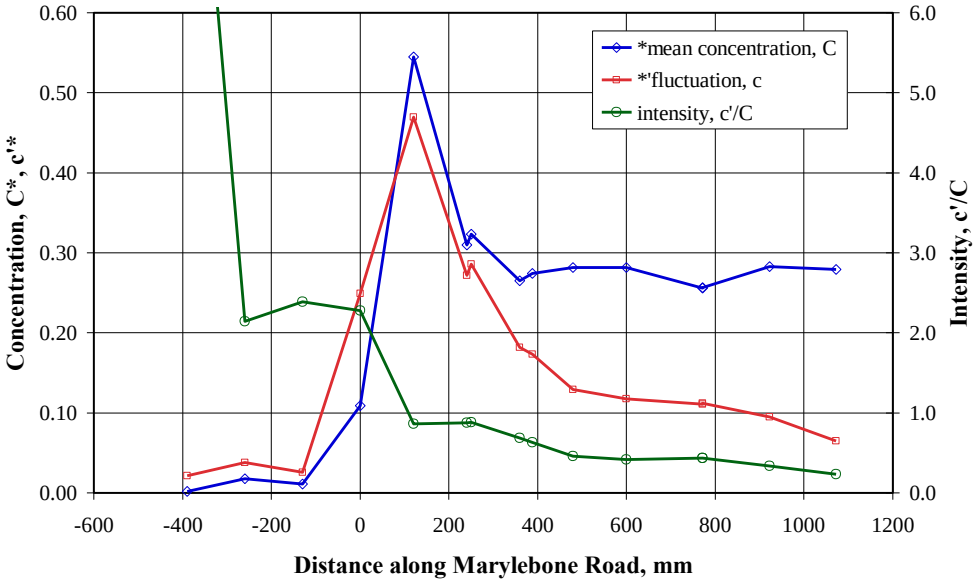

b) Mean and fluctuating dimensionless concentration distributions at street level along Marylebone Road for a ground level (10mm) emission.

Figure 3.16. Wind tunnel measurements of dimensionless concentrations (mean and fluctuation) at street level for emissions from three heights in York Street; wind direction 45˚ (from Smethurst, 2012). See Figure 5 for definitions of source location and co-ordinates.

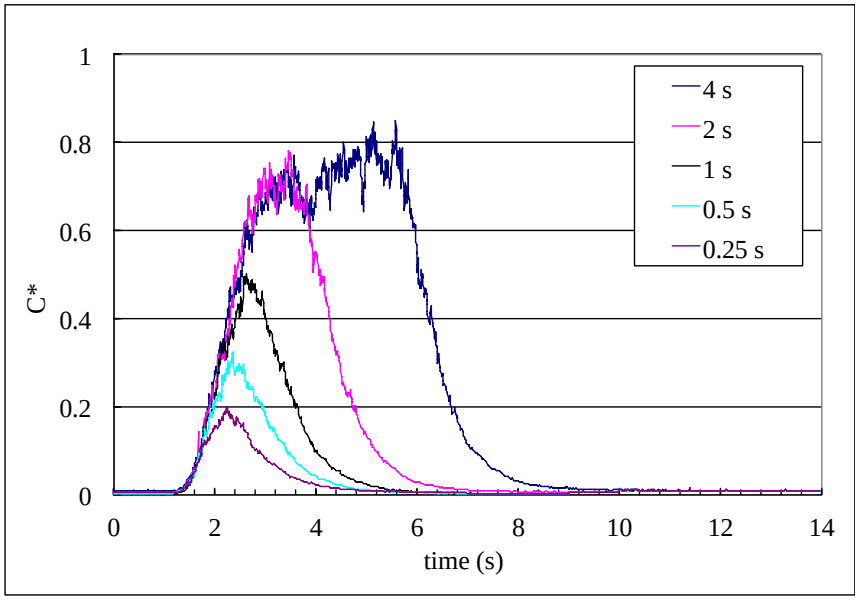

a) Ensemble averaged concentration series for different emission durations.

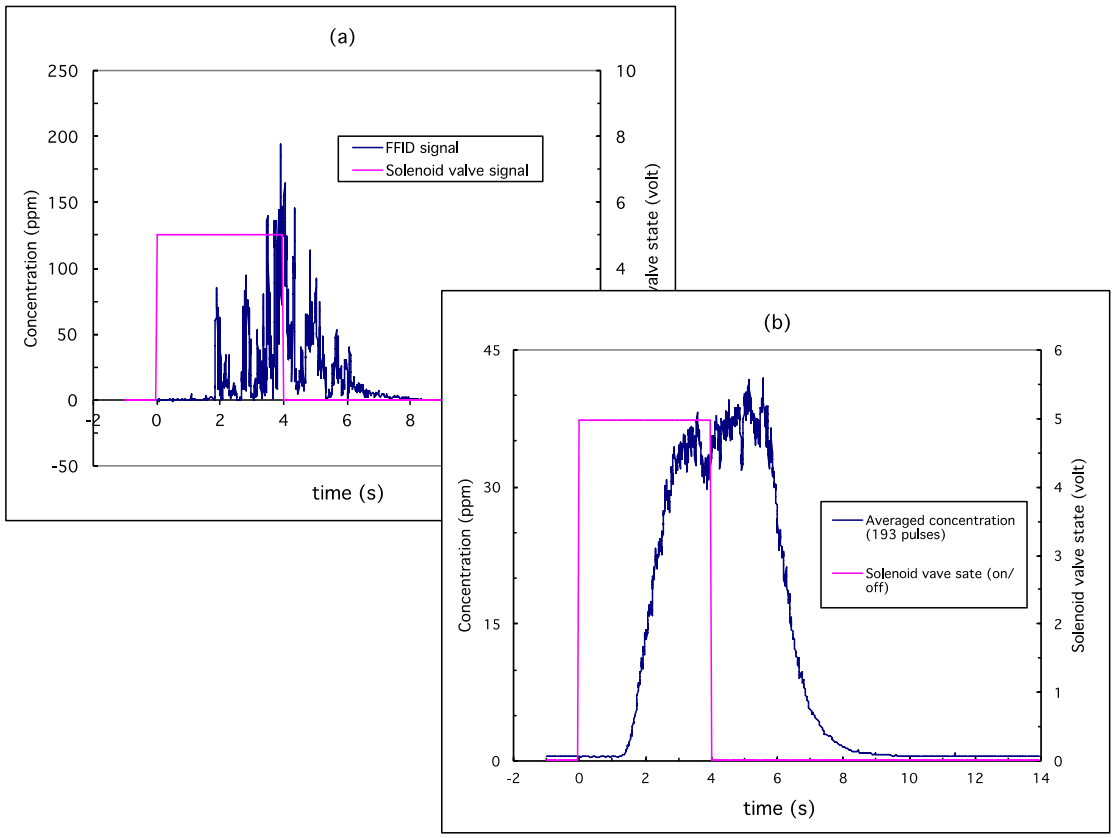

b) Ensemble average and single realisation for a 4s emission; the pink lines denote the source emission profile.

Figure 3.17. Concentration time series at a fixed location at street level in Marylebone Road, 7H from a ground level source in York Street, as shown in Figure 5; wind direction 45˚ for emission durations between 0.25 and 4s. (unpublished DAPPLE wind tunnel data)

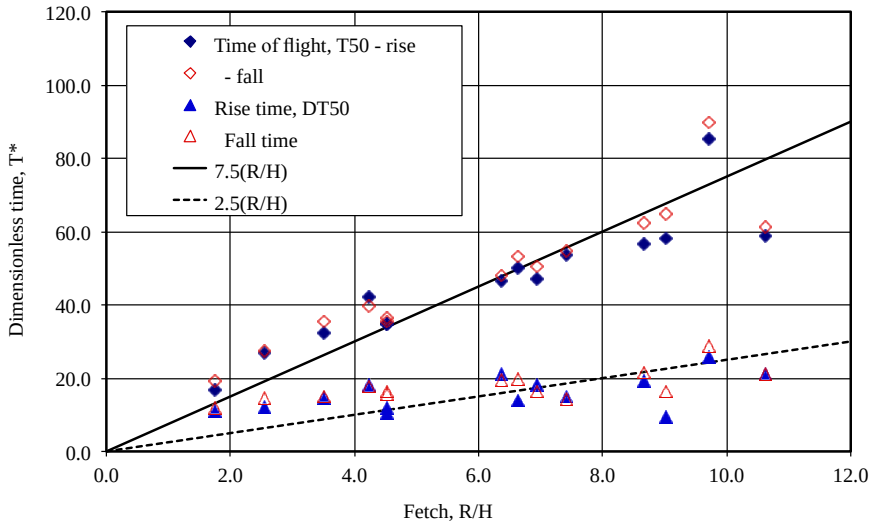

a) Time of flight, and concentration rise and fall times.

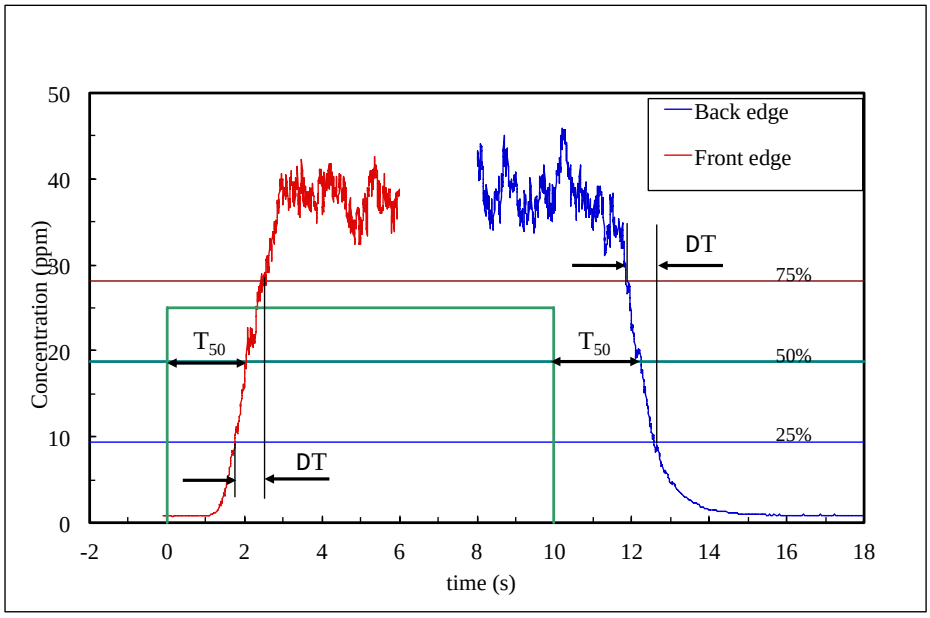

b) Definitions of travel times, T_{50} and rise and fall times, DT.

Figure 3.18. Time of flight based on cloud arrival and departure times, and concentration rise and fall times at street level as a function of distance from a ground level source in York Street (see Figure E5), wind direction 45˚. a) time scales; b) definitions. (unpublished DAPPLE wind tunnel data).

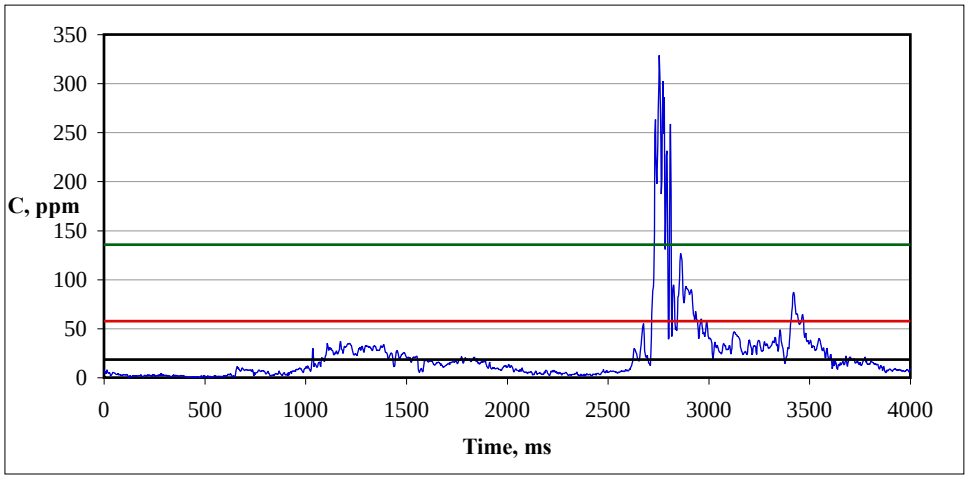

a) Location A

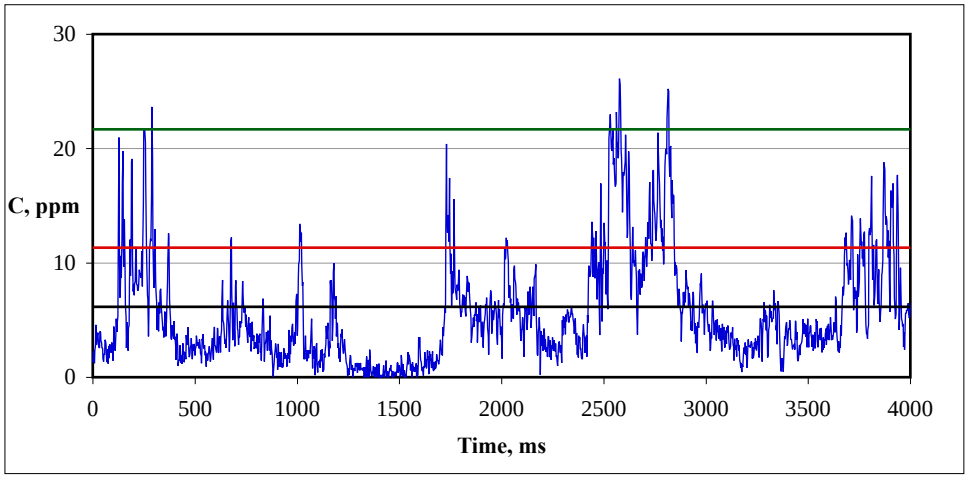

b) Location B

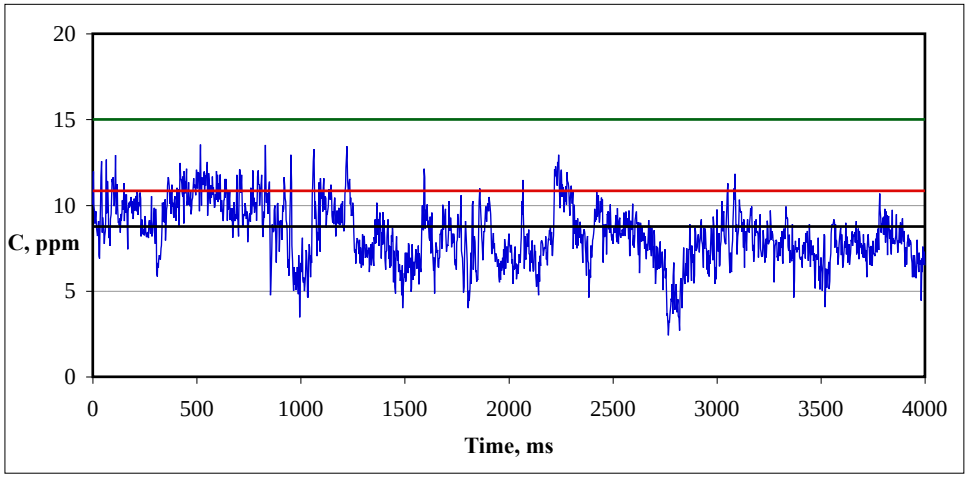

c) Location C

Figure 3.19. Samples of concentration time histories at street level locations A, B and C (see Figure 3.14) for a ground level source in York Street, wind direction 45˚ (Smethurst, 2012). Black line, mean value; red, mean plus standard deviation; green, mean plus three standard deviations.

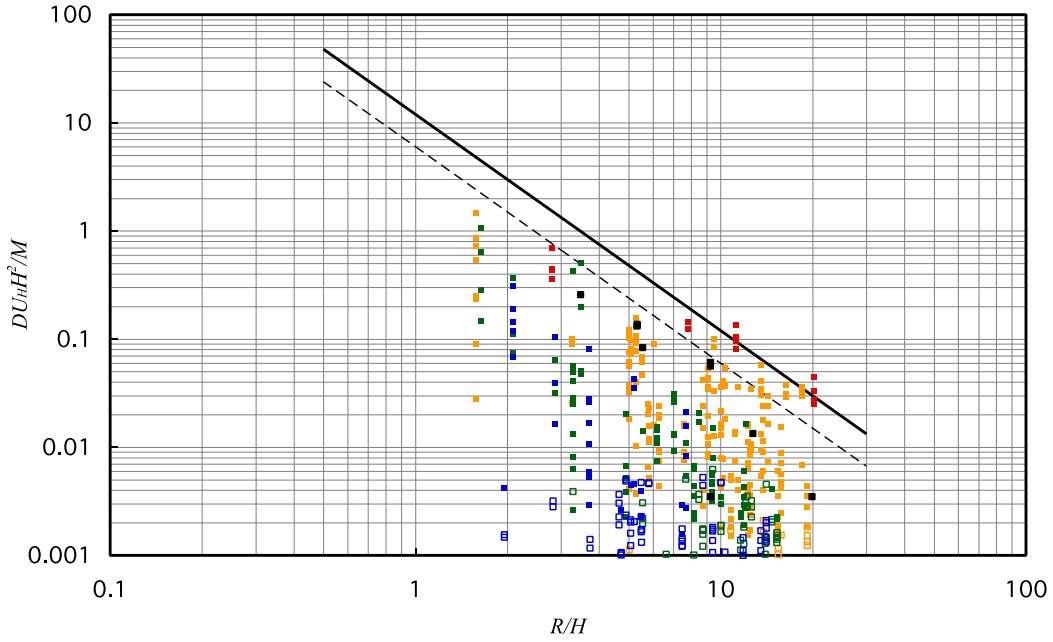

a) Field data from summer 2007.

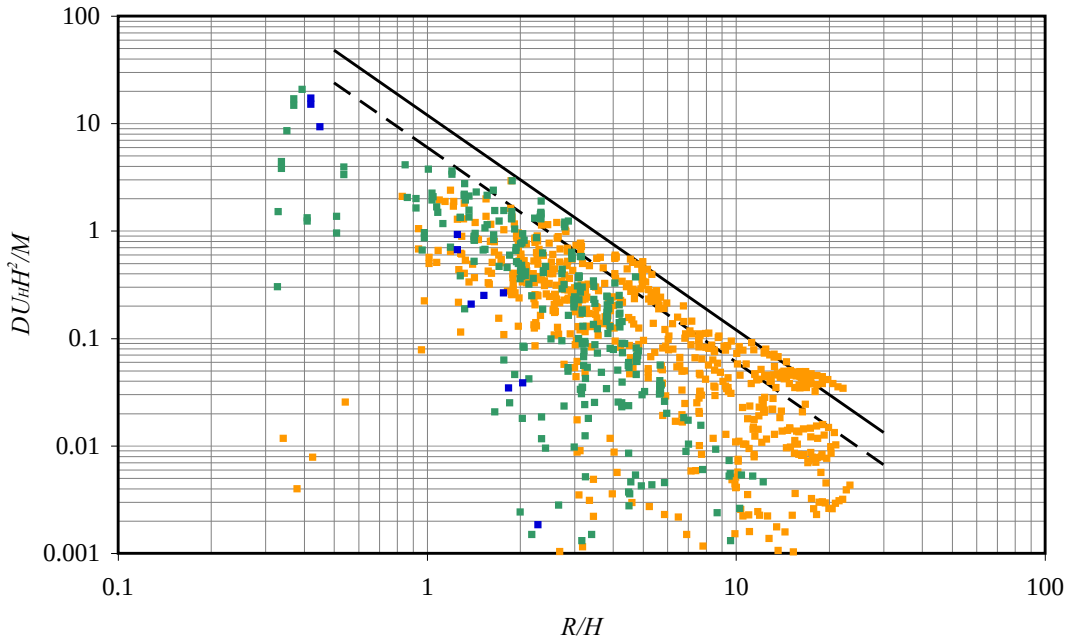

b) Wind tunnel data for wind direction 50˚.

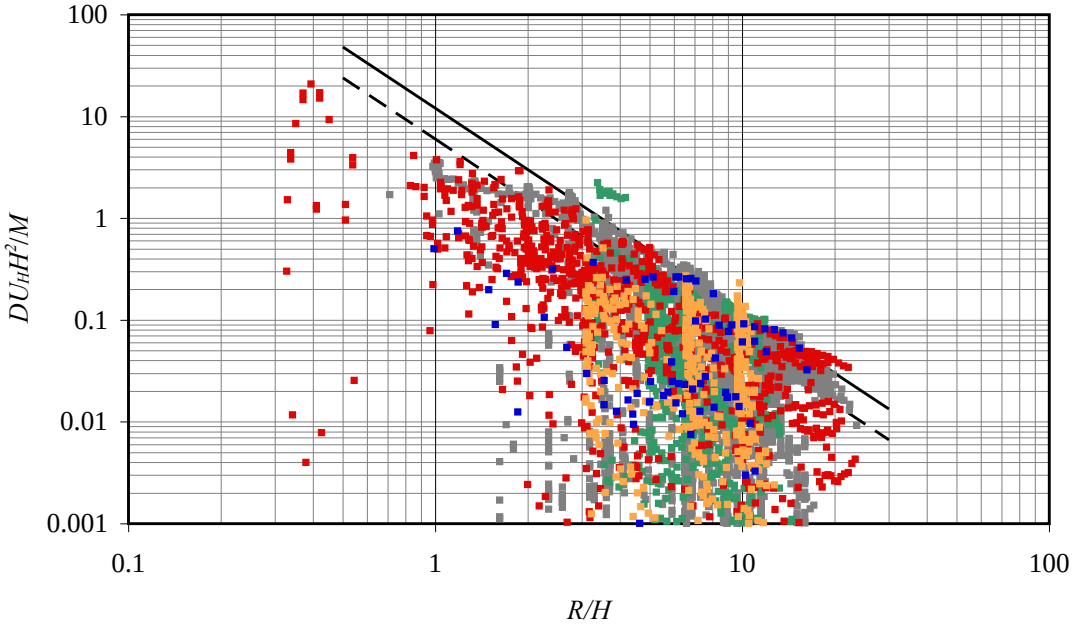

c) All wind tunnel data.

Figure 3.20. Variation of normalized dosage with normalized distance from the source measured in (a) full-scale experiments and (b) and (c) 1:200 scale wind tunnel experiments. Black points in (a) are from day 4. Coloured points in (a) show full scale data from days 1-3 and in (b) wind tunnel data for a wind direction of 50^o, both colour coded according to receptor location (see inset to (a)): red: channelled flow from source to receptor; yellow: receptor downwind of source; green: receptor across the wind from source; blue: receptor upwind of source. (c) All wind tunnel data colour coded according to wind direction: grey: 45^o; green: 90^o; red: 50^o; orange: 270^o blue: 114^o. The black lines show the empirical correlation (1) for the upper bound: solid: A = 12; dashed: A = 6. (DAPPLE, 2012)

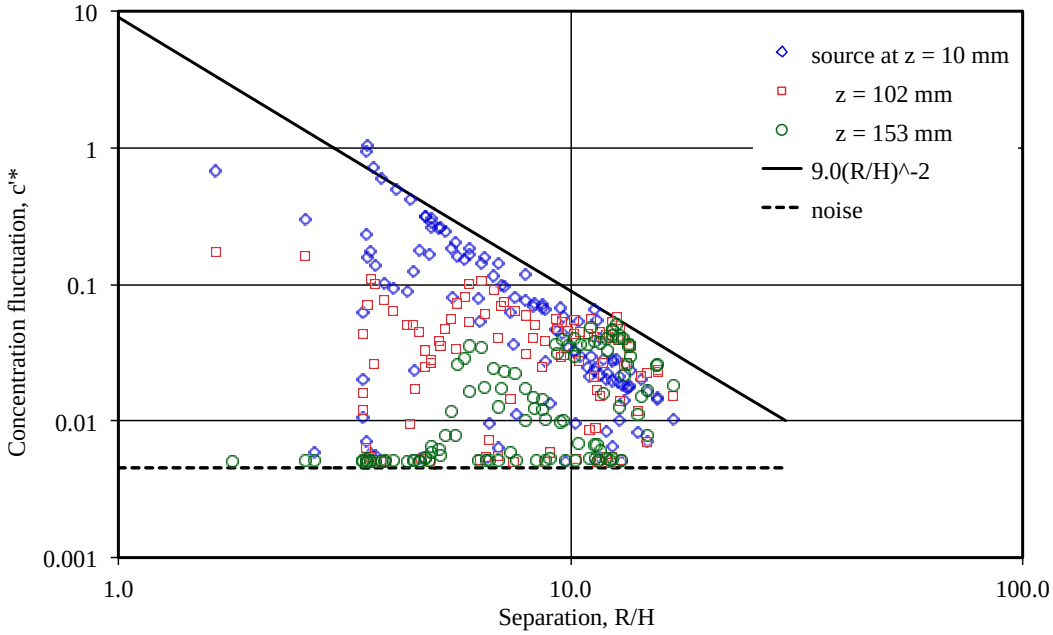

Figure 3.21. Variation of dimensionless standard deviation of concentration fluctuations at street level as a function of distance from emissions in York Street at heights of 10, 102 and 153mm, wind direction 45˚, compared with power-law fit to upper bound. The lower bound is defined by instrument noise. (Smethurst, 2012)

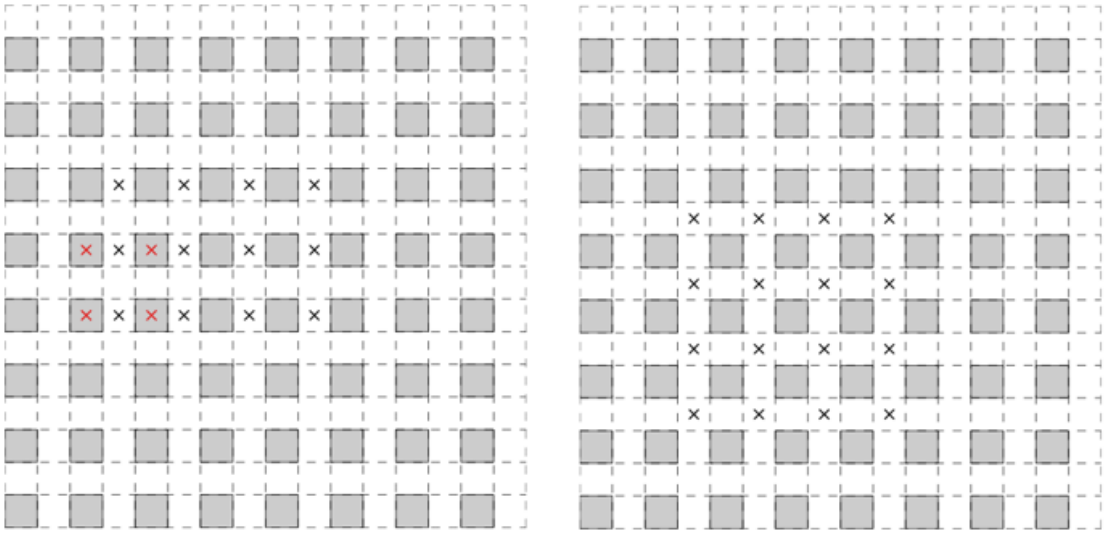

Figure 3.22. Plan view of computational domain in the DNS of Branford et al. (2011). Crosses denote the locations of an ensemble of ground-level sources. (a) 0° forcing direction (b) 45° forcing direction.

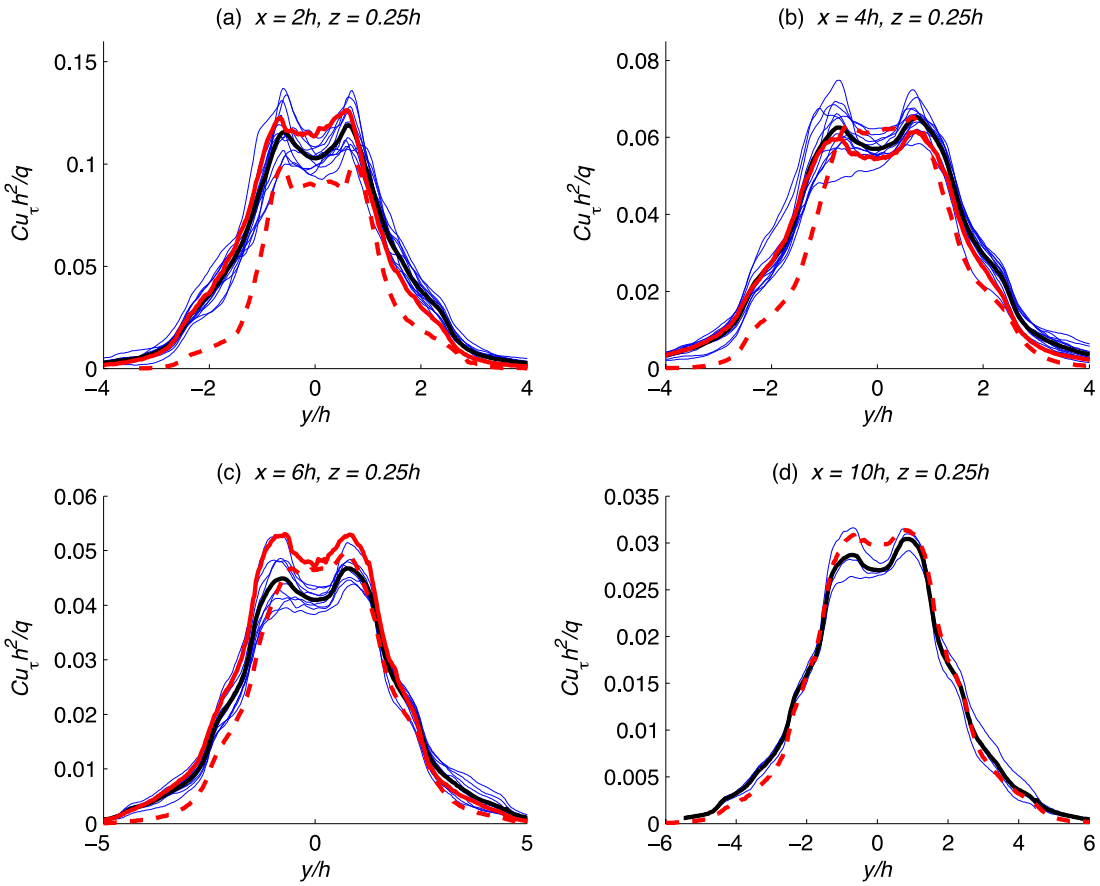

Figure 3.23. Ensemble-averaged mean concentration profiles from the 0° DNS run (black lines) compared with water channel data from Hilderman and Chong (2007) (solid red lines) within the array at four distances of 2H, 4H, 6H and 10H from the source. The blue lines are profiles from the individual releases comprising the ensemble of sources indicated by the black crosses in Fig. 3.22. The dotted red lines are measured profiles with a source close to the upstream edge of the array. Adapted from Branford et al. (2011).

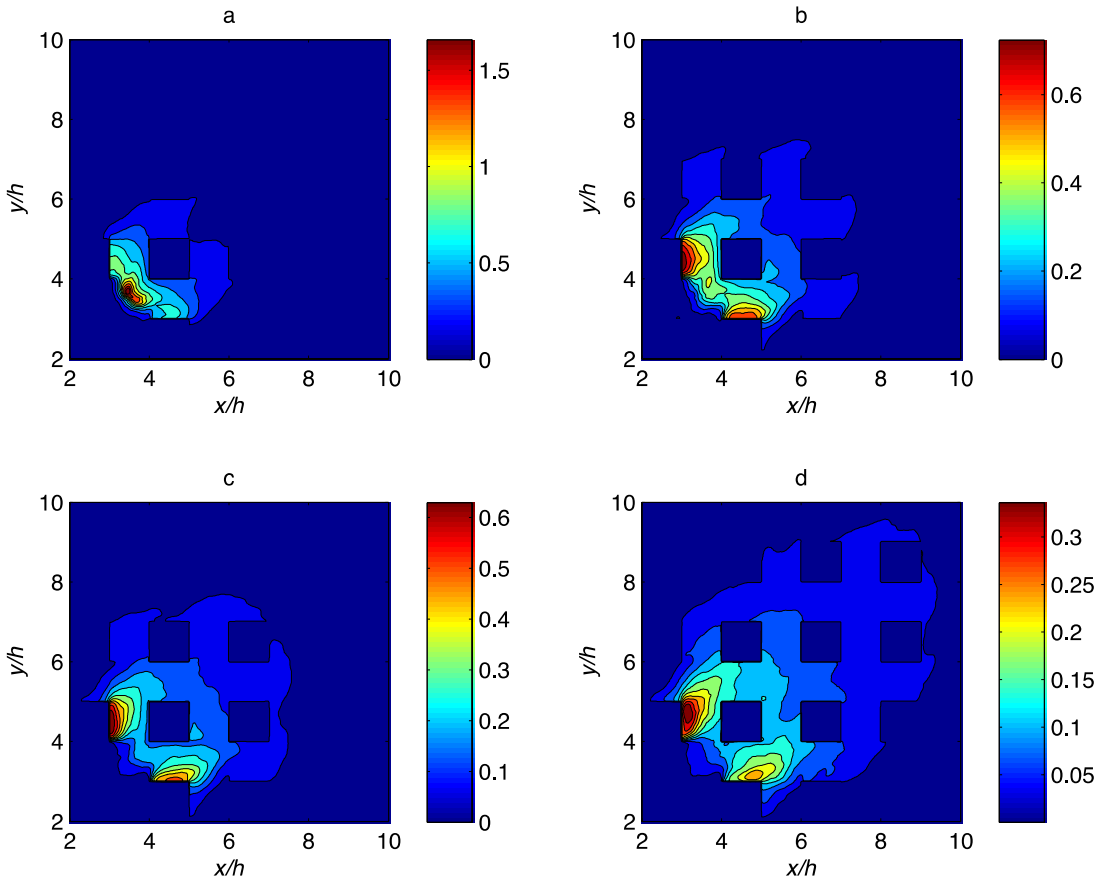

Figure 3.24. Contours of mean concentration at four different heights (0.25H, 0.5H, 0.75H and 1.0H) within the DNS array of Branford et al. (2011) for the 45° run, showing the accumulation of material from an initial release in an intersection into the wakes of adjacent buildings, giving rise to secondary wake sources.

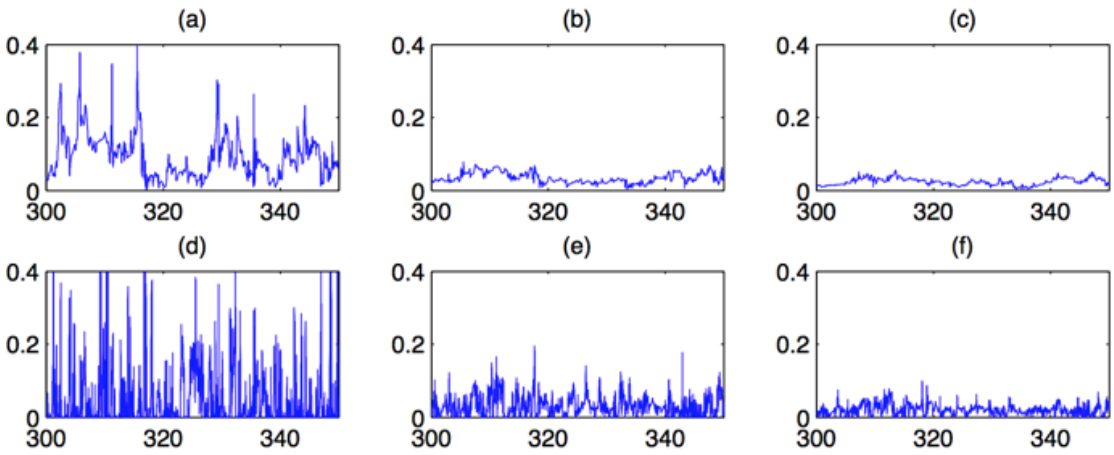

Figure 3.25. Time series of instantaneous concentration at selected locations within the array (at z = 0.25h) and above the array (at z = 1.25h) for a flow angle of 0◦ . Each row (e.g. sub-plots a, b and c in row 1) show the concentration at x = 2h, 6h and 10h respectively from the source. *Row 1:* between cubes in the array. *Row 2:* corresponding locations above the array. From Branford et al. (2011).

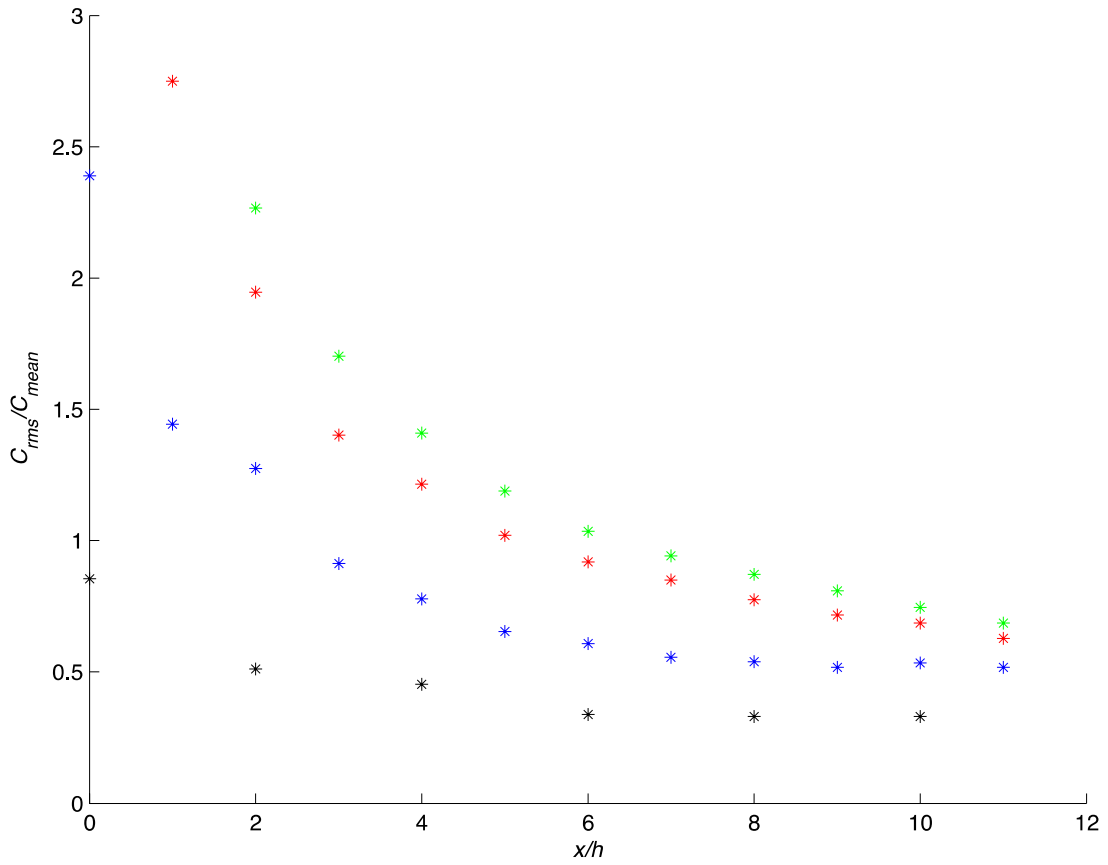

Figure 3.26. Relative concentration fluctuations c_{rms}/C_{mean} as a function of downstream distance from the source. Black and blue: locations within the array (z = 0.25H); Red and green: locations above the array (z = 1.25H). From Branford et al. (2011).

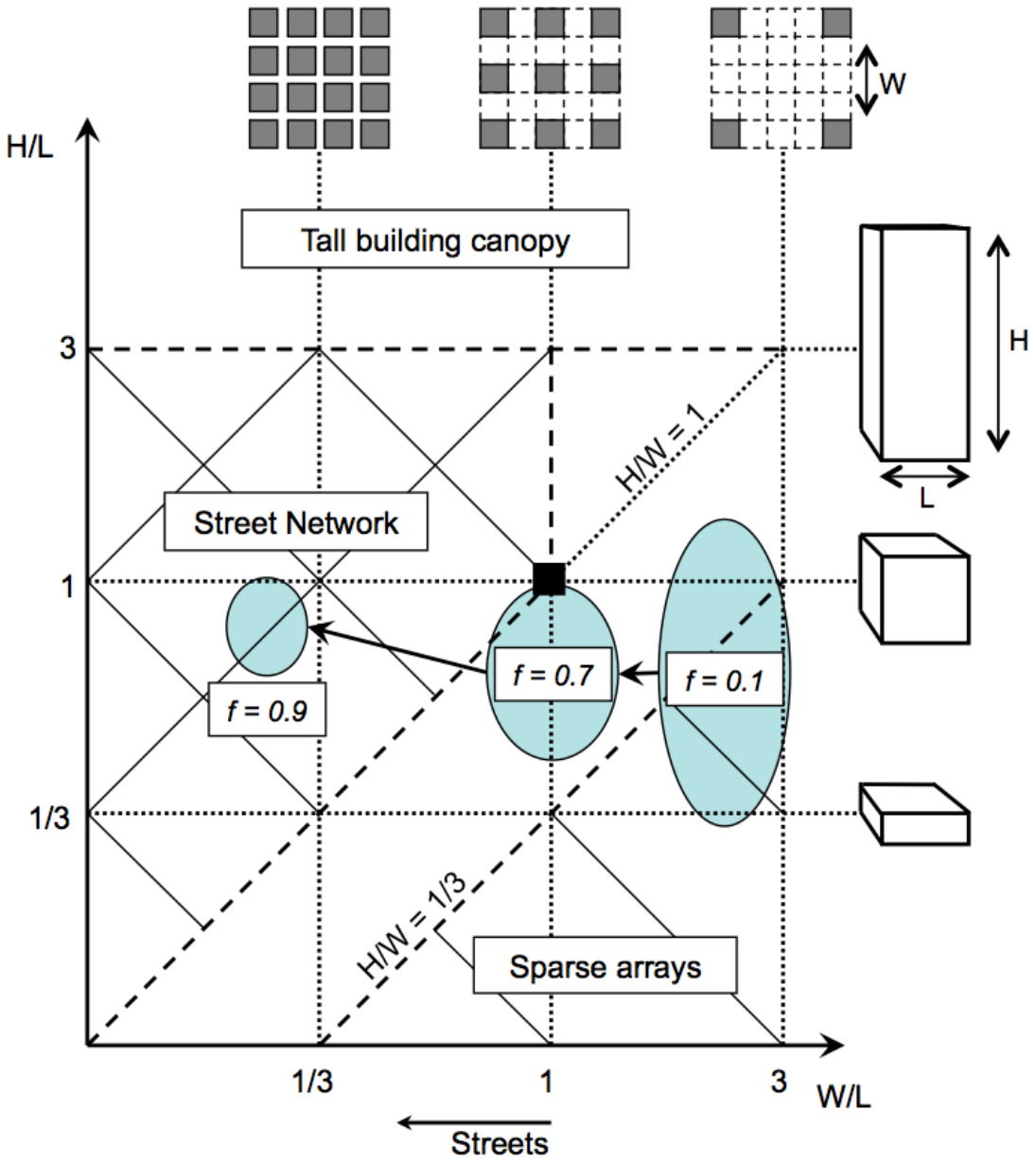

Figure 4.1. Regime diagram for dispersion through regular arrays of cuboids of base *L* x *L*, height *H* and separation *W*.

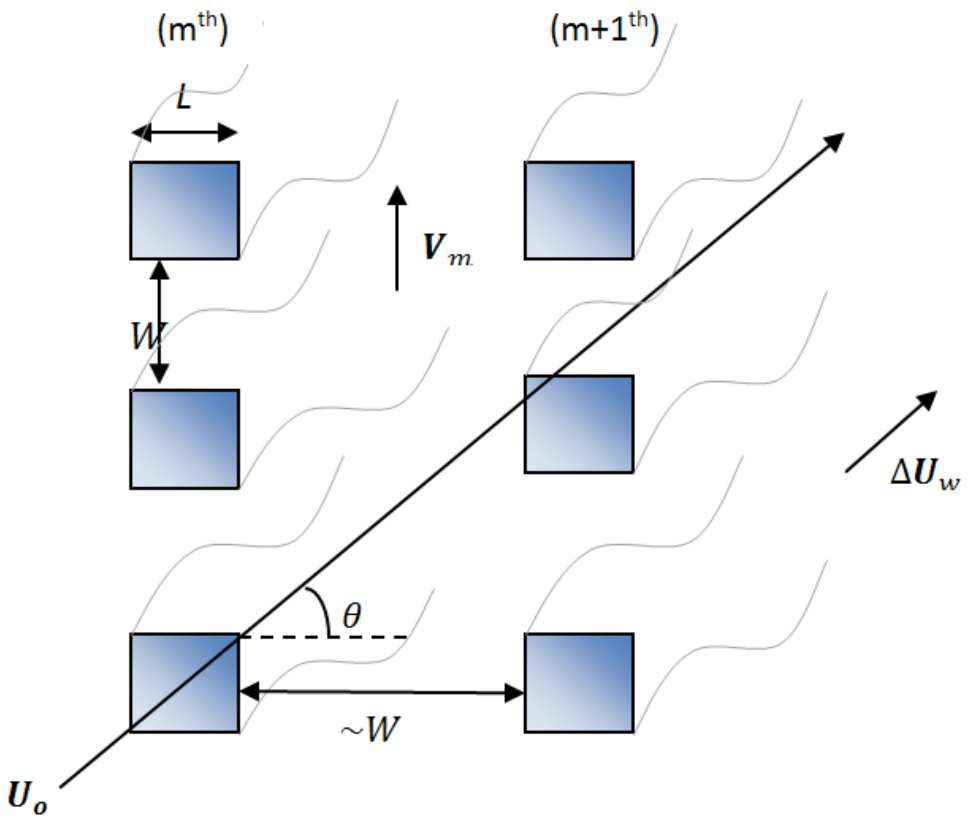

Figure 4.2. Building wakes with superposition but no significant interaction.

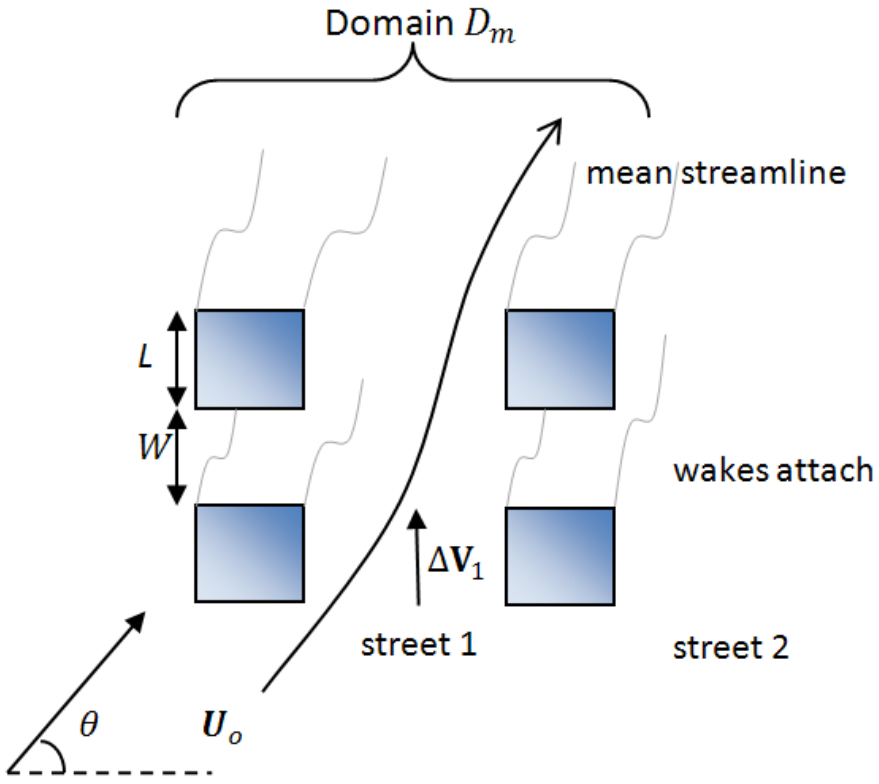

Figure 4.3. Flow with interaction between wakes

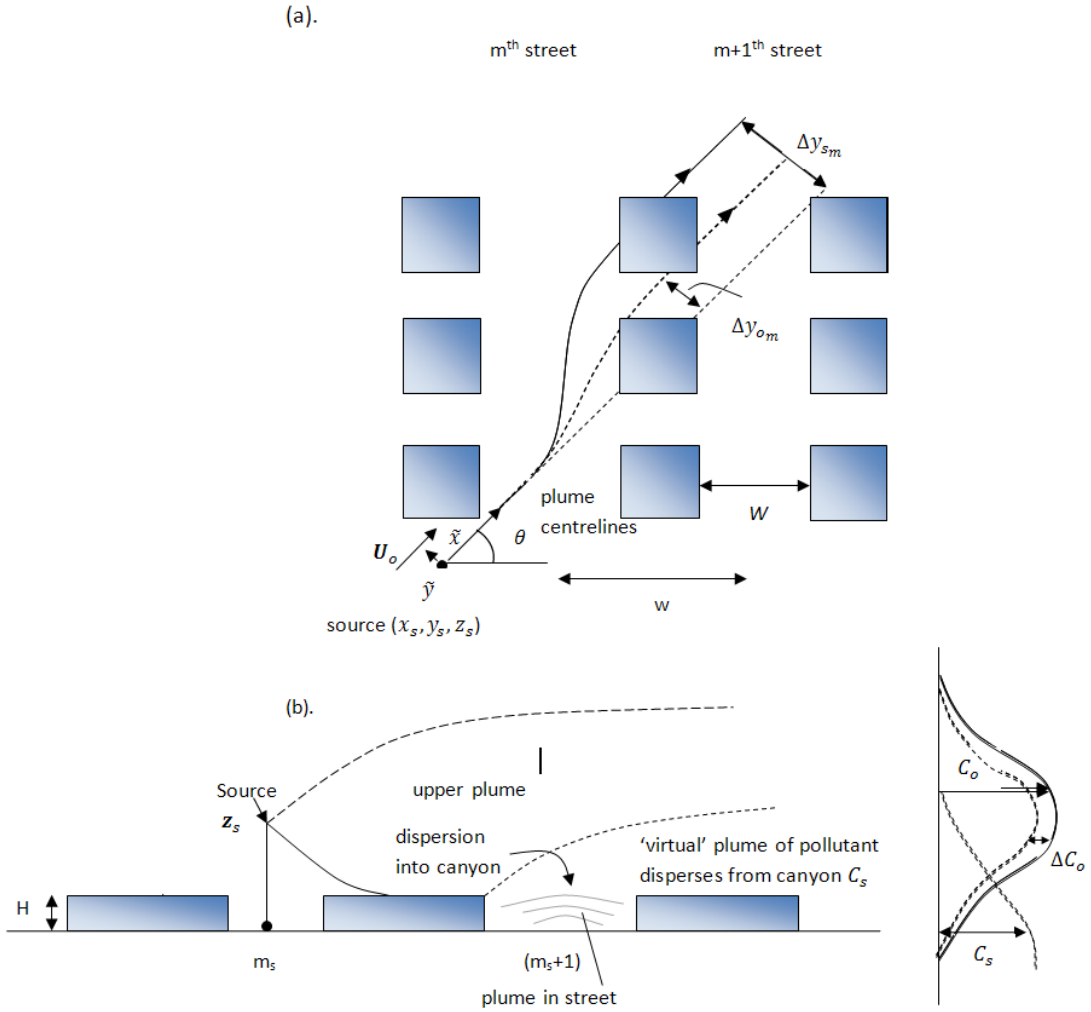

Figure 4.4. Dispersion from an upwind source (height $z_s > H$) in streets with significant canyon flows. Schematic shows difference between plume centreline displacement within the mth street, $\Delta\tilde{y}_{s_m}$, and above the mth street, $\Delta\tilde{y}_{o_m}$. (a) plan view (b) cross section. There are further smaller displacements in subsequent streets.

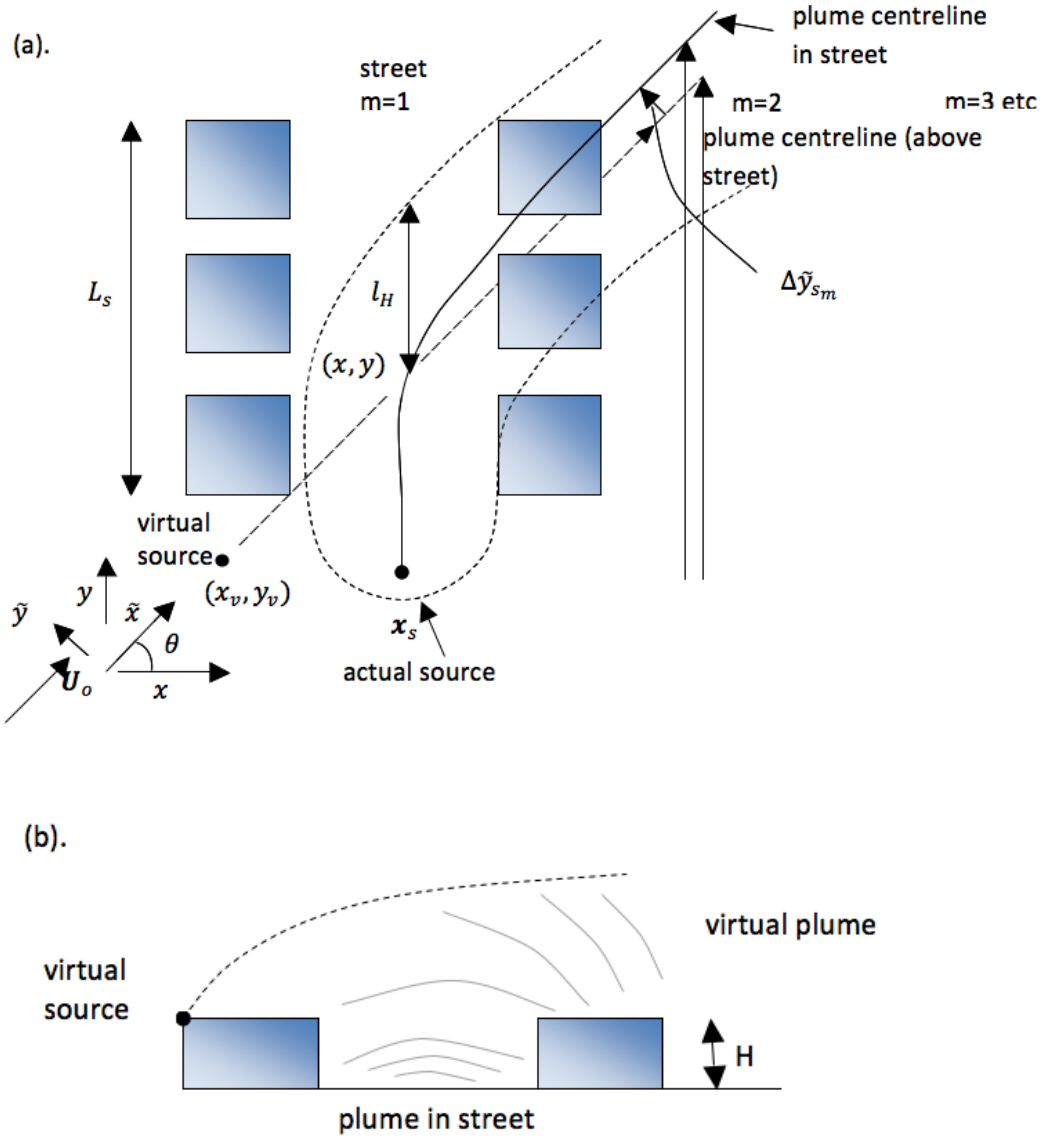

Figure 4.5. Dispersion in and above street with significant canyon flows. Source in street at x_s, y_s. Virtual source at x_v, y_v, z_v. Note $(x_v, x_s) \sim H$. Plume centreline displacement is $\Delta\tilde{y}_{o_m}$ above H, $\Delta\tilde{y}_{s_m}$ below *H.* (a) plan view (b) cross section.

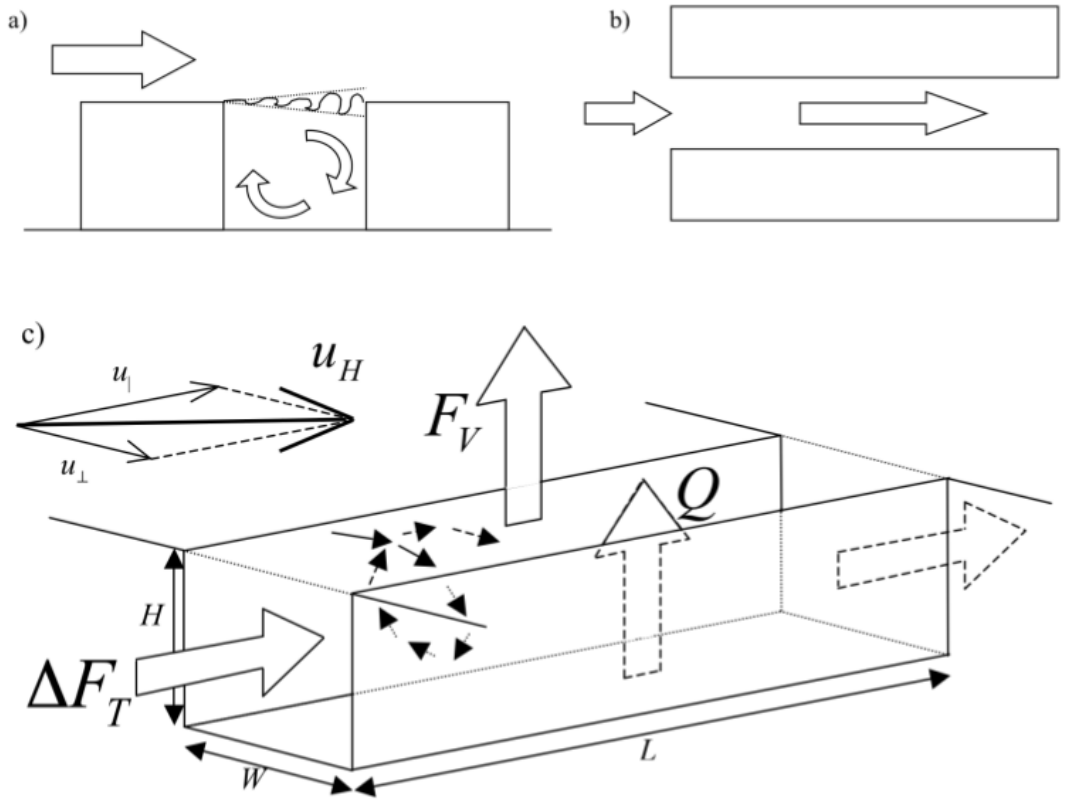

Figure 4.6. Mixing and transport in a simple street. a) Side view of wind blowing perpendicular to the street, which drives a mixing circulation in the street canyon. The wavy line at roof level indicates the instantaneous interface between fast moving above roof air and slower moving street canyon air. b) Plan view of wind blowing parallel to the street, which drives a channelling flow along the street. c) Perspective view of when the wind at roof level, u_H, has a component, $u_{||}$, parallel to the street, which drives a flow along the street, and a component, $u_{|}$, perpendicular to the street, which drives a circulation across the street. Air parcels then move in helical paths as indicated by the arrows. The large arrows indicate fluxes in the volume averaged pollution budget. Taken from Belcher (2005)

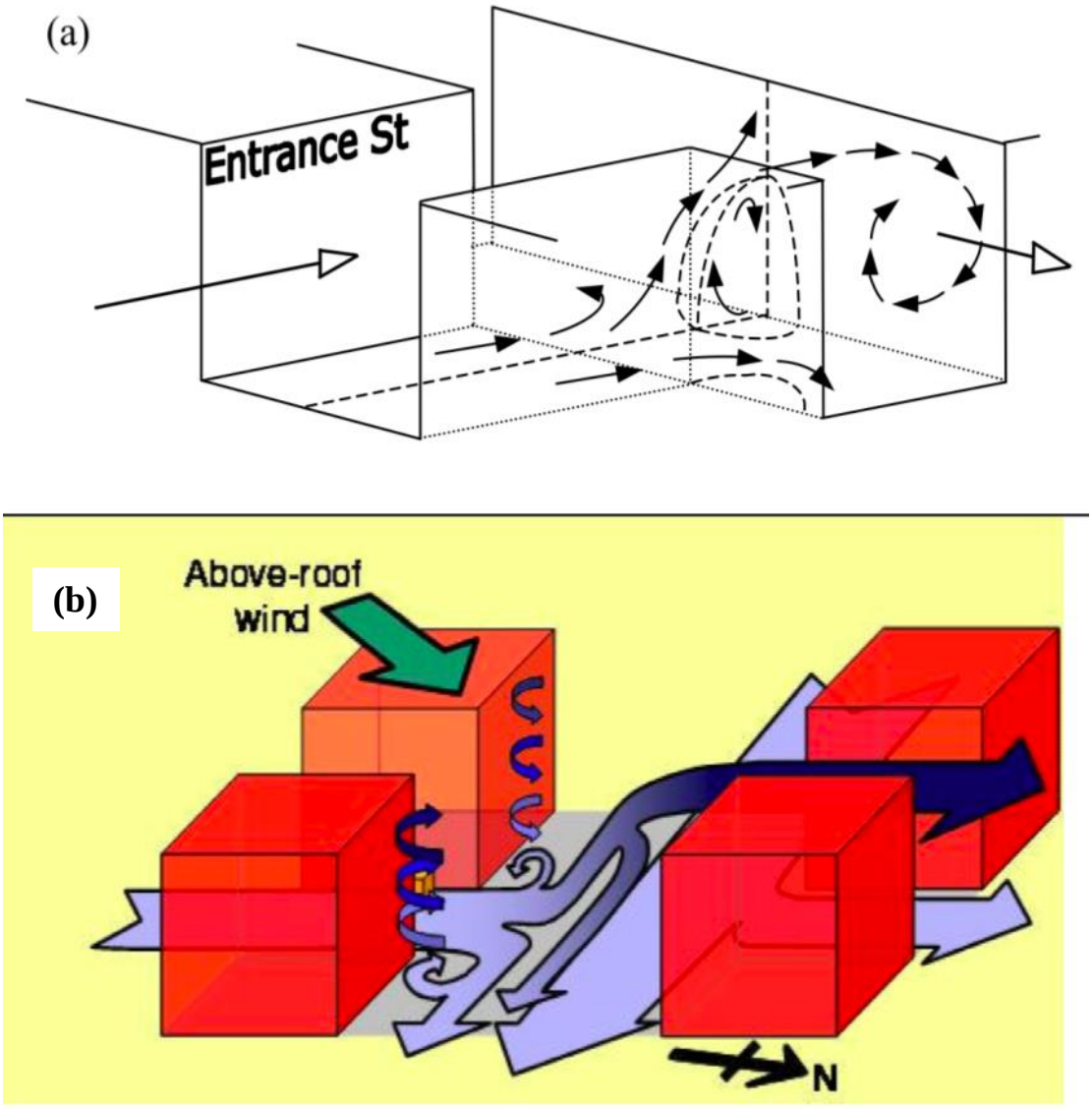

Figure 4.7. Mixing and transport at a street intersection. (a) Flow pattern at a T-junction (taken from Belcher 2005) (b) Flow pattern at a four-way junction (taken from Wood et al. 2010).

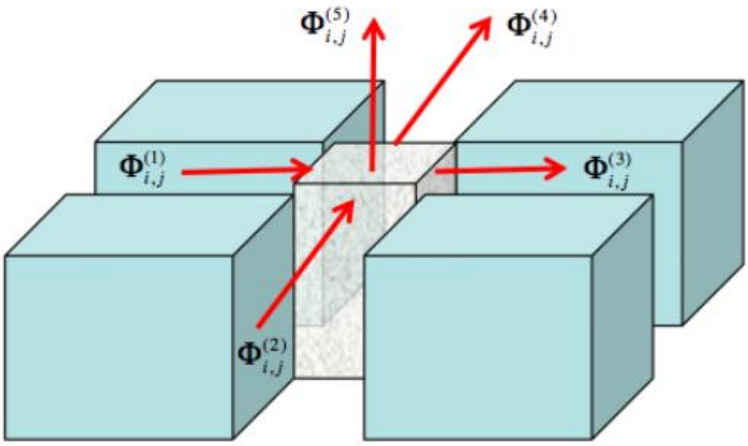

Figure 4.8. Schematic showing the five fluxes into and out of a 4-way street intersection.

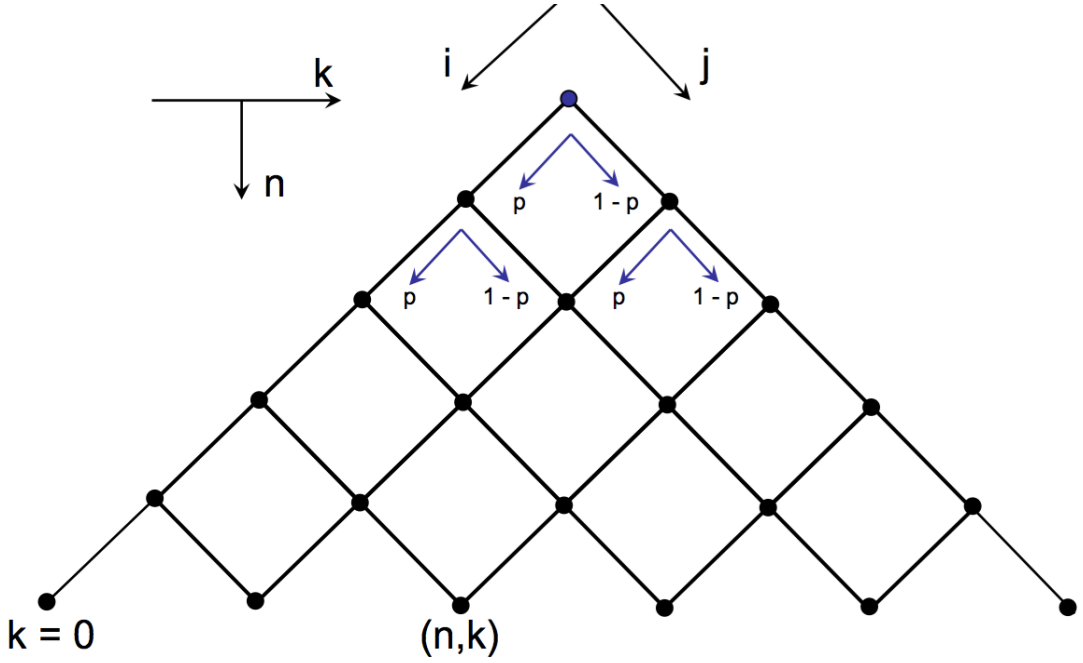

Figure 4.9. Schematic diagram showing the network of intersections (represented by points) and the connecting streets (represented by the lines) of the simple street network. At each intersection a fraction, *p*, of material is advected to the right and a fraction (*1-p*) of material advected to the left. The motion through the network then resembles the passage through a branching network, albeit with a loss of a fraction (1 – *α*) of material through each intersection.

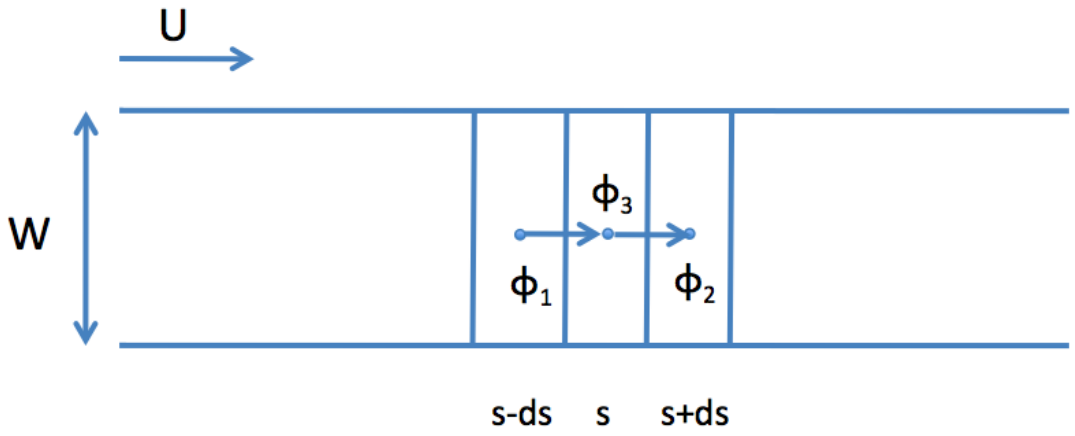

Figure 4.10. Flux balance in a long street. W is the street width and U is a characteristic advection velocity along the street. See text for further explanation.

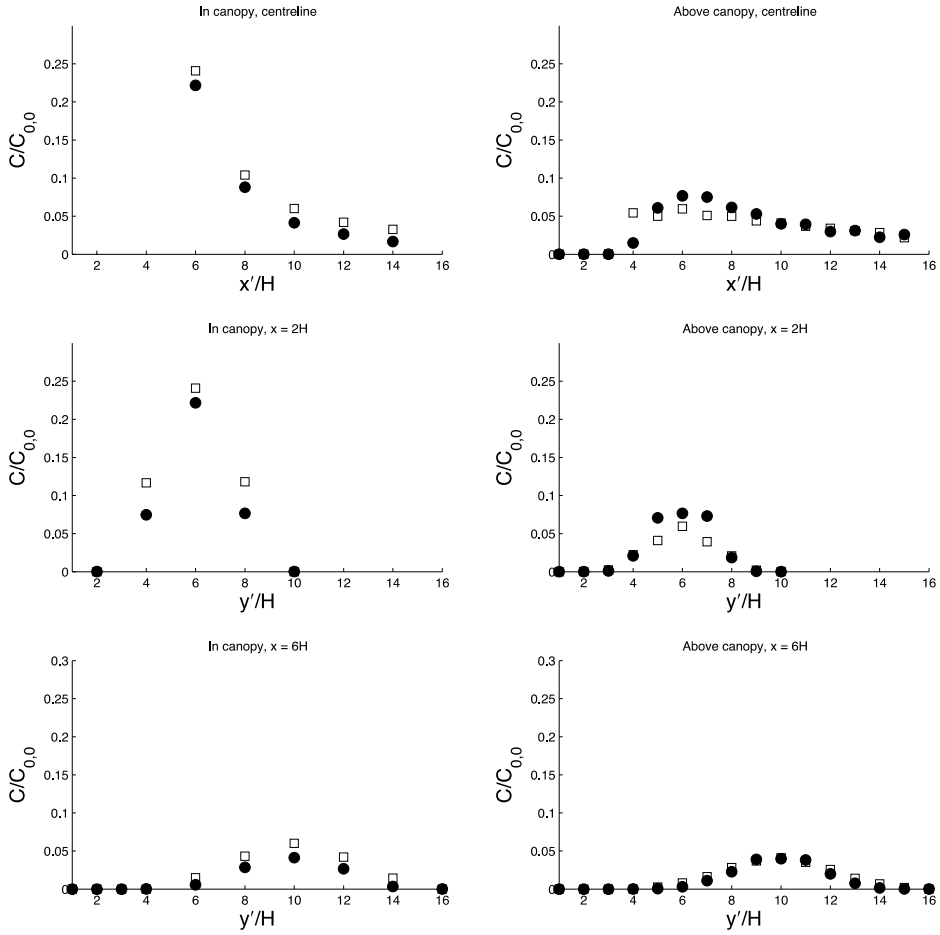

Figure 4.11. Comparison of network model predicted concentrations (squares) with DNS data (filled circles) for centreline and lateral profiles within the canopy (left) and above the canopy (right). Adapted from Goulart (2012).

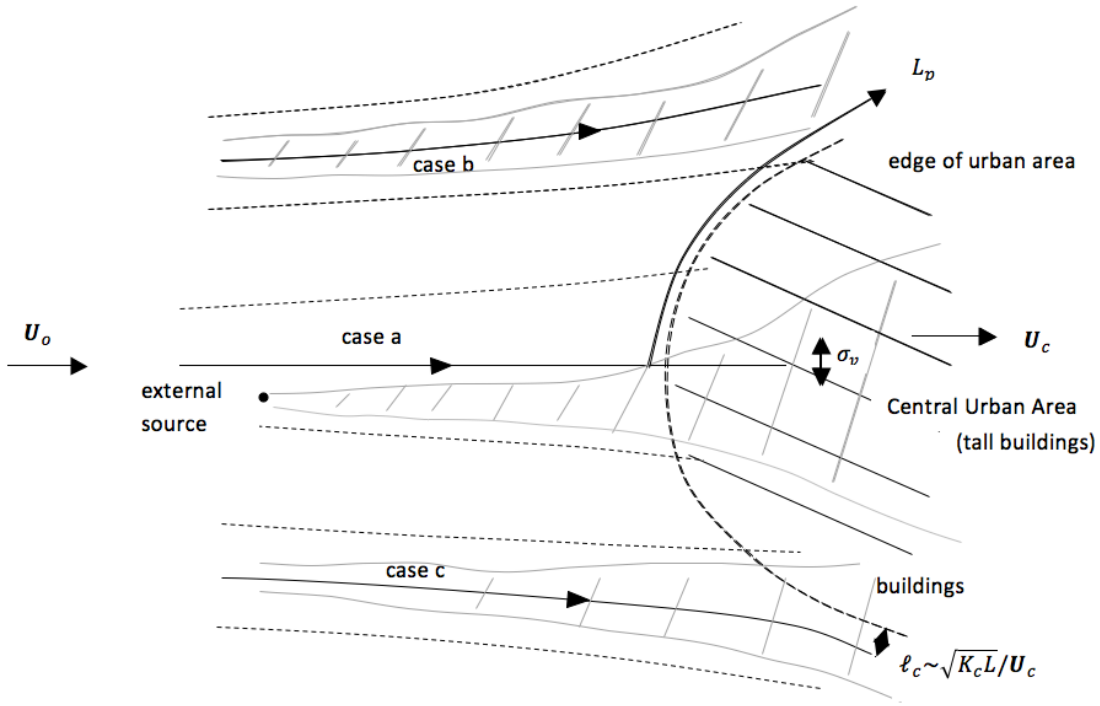

Figure 4.12. Flow streamline below the building heights as the wind enters and passes round the urban area

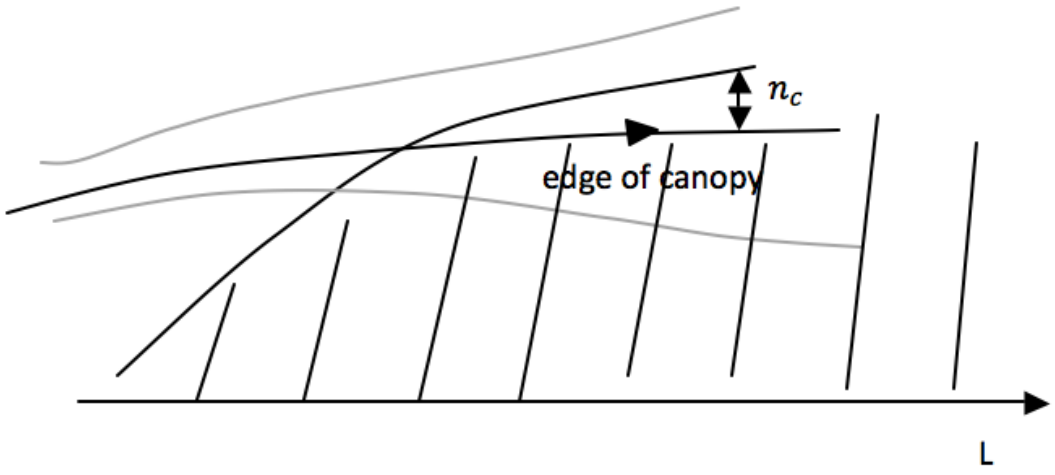

Figure 4.13. Plume approaches edge of urban area tangentially

Tracer-day		1	2	3	4
Date		31/5/07	7/6/07	8/6/07	28/6/07
Sensible heat flux, Wm^{-2}	BT Tower	240	90	290	100
Monin-Obhukov scale, m	BT Tower	-140	-70	n/a	n/a
Mean wind speed, ms^{-1}	BT Tower	7.0 ± 1.2	5.9 ± 1.0	3.1 ± 1.2	8.6 ± 1.0
	Roof top	3.0 ± 1.7	1.9 ± 1.2	1.2 ± 0.9	2.6 ± 1.7
Mean wind direction, degs	BT Tower	+75	-133	-125	+28
	Roof top	+83	-122	-120	+35

Table 1. Summary of 30-minute mean flow conditions for 2007 tracer-day periods (typically 11:00–13:30 UTC). The results indicate that a slight to moderately unstable boundary layer occurred on all four days. Wind speed data are shown with ± 1 standard deviation computed from 20 Hz ultrasonic anemometer data.

Model	Approach	Availability	Documentation	GUI	Urban input data	Met. input data and parametrization
UDM	Gaussian	Not available	Not available	Yes	Urban array parameters	Minimum met input: wind speed and direction, stability.
ADMS-Urban	Street canyon	Commercial license	Yes – online	Yes	Street canyon dimensions	Monin-Obukhov similarity; Minimum met input: wind speed and direction and either Monin-Obhukhov length or sensible heat flux or cloud cover, time and date.
SIRANE	Street network	Commercial license	Yes	No	Street dimensions and street network topology	Monin-Obukhov similarity; Minimum met input; wind speed and direction, surface temperature and time and date. Roughness length and displacement height estimated using empirical methods (Macdonald et al. 1998).
QUIC	Building resolving	By permission	Yes – online	Yes	Complete building geometry	Wind profile and wind direction.

Table 2. Examples of software packages used for urban dispersion modelling based on different approaches